Analysis of the Evolution of a Multi-Ribbon Flare and Failed Filament Eruption

Reetika Joshi[1,2,3] (ID) · **Cristina H. Mandrini**[4] (ID) · **Ramesh Chandra**[3] (ID) ·
Brigitte Schmieder[5,6,7] (ID) · **Germán D. Cristiani**[4] (ID) · **Cecilia Mac Cormack**[4] (ID) ·
Pascal Démoulin[5,8] (ID) · **Hebe Cremades**[9,10] (ID)

Abstract

How filaments form and erupt are topics about which solar researchers have wondered for more than a century and they are still open to debate. We present observations of a filament formation, its failed eruption, and the associated flare (SOL2019-05-09T05:51) that occurred in active region (AR) 12740 using data from the Solar Dynamics Observatory (SDO), the Solar-Terrestrial Relations Observatory A (STEREO-A), the Interface Region Imaging Spectrograph (IRIS) and the Learmonth Solar Observatory (LSO) of the National Solar Observatory/Global Oscillation Network Group (NSO/GONG). AR 12740 was a decaying region formed by a very disperse following polarity and a strong leading spot, surrounded by a highly dynamic zone where moving magnetic features (MMFs) were seen constantly diverging from the spot. Our analysis indicates that the filament was formed by the convergence of fibrils at a location where magnetic flux cancellation was observed. Furthermore, we conclude that its destabilisation was also related to flux cancellation associated with the constant shuffling of the MMFs. A two-ribbon flare occurred associated with the filament eruption; however, because the large-scale magnetic configuration of the AR was quadrupolar, two additional flare ribbons developed far from the two main ones. We model the magnetic configuration of the AR using a force-free field approach at the AR scale size. This local model is complemented by a global potential-field source-surface one. Based on the local model, we propose a scenario in which the filament failed eruption and the flare are due to two reconnection processes, one occurring below the erupting filament, leading to the two-ribbon flare, and another one above it between the filament flux-rope configuration and the large-scale closed loops. Our computation of the reconnected magnetic flux added to the erupting flux rope, compared to that of the large-scale field overlying it, allows us to conclude that the latter was large enough to prevent the filament eruption. A similar conjecture can be drawn from the computation of the magnetic tension derived from the global field model.

Keywords Heating, coronal · Magnetic fields, coronal · Flares, dynamics

1. Introduction

Solar filaments are clouds of cool and dense plasma suspended against gravity by forces thought to be of magnetic origin. Filaments appear in Hα, Ca II images as dark features on

the disk and as bright loops at the limb; this is well explained by absorption and emission mechanisms. Prominences are bright also in transition-region lines (He II 304 Å) mapping the prominence–corona transition region, but dark in some extreme-ultraviolet (EUV) filter-grams due to continuum photoionisation phenomena, *e.g.* Fe XI 171 Å (Labrosse et al., 2010). The main plasma characteristics of prominences are reviewed in Labrosse et al. (2010), while their magnetic properties are discussed in the articles by Mackay et al. (2010) and Gibson (2018).

Prominences form along the magnetic polarity inversion line (PIL) in or between active regions. Early observations already suggested that their fine structure is apparently composed by many horizontal and thin dark threads (Leroy, Bommier, and Sahal-Brechot, 1983; Bommier, Sahal-Brechot, and Leroy, 1986; Tandberg-Hanssen, 1995), as has been confirmed by observations using several telescopes, *i.e.* the Télescope Héliographique pour l'Etude du Magnétisme et des Instabilités Solaires (THEMIS) (López Ariste et al., 2006; Schmieder et al., 2014; Levens et al., 2016), the Solar Optical Telescope (SOT) on the Hinode satellite (Berger et al., 2008) and the New Vacuum Solar Telescope (NVST, Shen et al., 2015). Some fine nearly horizontal plasma structures, lying in magnetic dips above parasitic polarities located in the filament channel, form the filament feet or barbs, while the endpoints are anchored in the background magnetic field (López Ariste et al., 2006). The distance between these feet has a characteristic length comparable to the size of supergranules (30 Mm). Even if prominences appear sometimes as hanging vertically over the limb their global structure is almost horizontal (Martin, 1998; Chae et al., 2008). Dynamics and projection effects could be responsible of such non-real appearance (Schmieder et al., 2017).

Magnetic field extrapolations and magnetohydrodynamics (MHD) models have confirmed that the global structure of prominences consists of flux tubes or arcades of twisted magnetic field lines that have shallow dips in which cool plasma is trapped (Aulanier and Démoulin, 1998; van Ballegooijen, 2004). In this aspect, prominences can be the cores of coronal-mass-ejection (CME) flux ropes (Fan, 2015) and their eruptions are the drivers of flares (Devi et al., 2021), in general, of the two-ribbon type (see, e.g. the standard model of flares discussed in Aulanier et al., 2010; Schmieder, Démoulin, and Aulanier, 2013).

The review by Mackay et al. (2010, and references therein) discusses the formation mechanisms of prominences. Different models are proposed based on levitation, evaporation and condensation processes. More recently, Gibson (2018) describes the formation of prominences and the structure of the magnetic skeleton that supports and surrounds the prominence, as well as how the plasma and magnetic field dynamically interact. Magnetic reconnection between short filaments or chromospheric fibrils, sometimes accompanied by bidirectional jets (Tian et al., 2017; Shen et al., 2017; Ruan et al., 2019; Shen, 2021), may lead to the formation of long filaments (Schmieder et al., 2004, 2006; Wang and Muglach, 2007); when this process happens close to parasitic polarities it may favour the formation of barbs. Such magnetic configurations correspond to the models proposed by van Ballegooijen and Martens (1989).

High-resolution observations of coronal jets, mostly of the blow-out kind, have identified the presence and eruption of small-scale filaments, called mini-filaments, as being part of the ejected material (Hong et al., 2011; Shen, Liu, and Su, 2012; Sterling et al., 2015, 2016; Panesar, Sterling, and Moore, 2017; Yang and Zhang, 2018; Moore, Sterling, and Panesar, 2018; Shen et al., 2019). In another example, based on the analysis of lower-resolution observations, the presence of a constantly reformed mini-filament and its eruption was proposed as the origin of a series of blow-out jets and the chain of events following them (flares and narrow CMEs, Chandra et al., 2017a). The mechanism associated with the destabilisation of the mini-filament, as also happens with well-developed filaments, was the cancellation of magnetic flux along the polarity-inversion line (PIL). Magnetic reconnection below

the mini-filament was responsible for an observed flare, while the same process above the mini-filament favoured the injection of its material into open field lines to form the blow-out jet. The identification of mini-filament eruptions as the main origin of the plasma ejected in these jets led Wyper, Antiochos, and DeVore (2017) and Wyper, DeVore, and Antiochos (2018) to propose that these ejections are produced by a break-out mechanism similar to the one proposed to explain larger events like CMEs (see Karpen, Antiochos, and DeVore, 2012). Several articles have reviewed different explanations (magnetic flux emergence and cancellation) for the origin of standard and blow-out jets using imaging and spectroscopic observations (see, e.g. Shen, 2021; Schmieder, 2022, and references therein).

In general, not all eruptions end in a CME; there are partial and failed eruptions. A number of flux ropes and the embedded prominences suffer the latter kind of ejection, which imply that at first they suddenly start to ascend, then decelerate, and stop rising at some larger height in the corona. Several cases of failed eruptions have been reported in the literature (Shen, Liu, and Su, 2012; Chen, Ma, and Zhang, 2013; Joshi et al., 2013; Cheng et al., 2015; Thalmann et al., 2015; Xue et al., 2016; Chandra et al., 2017b; Nisticò et al., 2017; Liu et al., 2018; Filippov, 2020, 2021). Chen, Ma, and Zhang (2013) and Xue et al. (2016) interpreted an unsuccessful eruption because of the presence of strong closed overlying EUV arcades. An asymmetry of the background magnetic field, considering only the relative location of the filament, has been suggested as the origin of failed eruptions (Liu et al., 2009). Joshi et al. (2013) studied the event of 17 June 2012; they discussed that the eruption of the flux rope and its filament could fail even after they reached up to the Large Angle and Spectrographic Coronagraph (LASCO) C2 field of view (FOV) and were visible as a CME. These authors associated the failed CME with an asymmetric filament eruption. Thalmann et al. (2015) concluded that the strong overlying magnetic field over the active region (AR) 12192 in October 2014 prevented any CME from occurring associated with X-class flares. A comparative study of eruptive and non-eruptive events was performed by Liu et al. (2018). These authors explained non-eruptive events proposing two possibilities: first, the active region non-potentiality and a weak Lorentz force could be responsible for the small momentum of the ejecta and, secondly, the torus-stability region confined the eruption (see Török and Kliem, 2005; Zuccarello, Aulanier, and Gilchrist, 2016, for a discussion on the role of the torus instability). Very recently, Filippov (2021) estimated the mass of fifteen failed eruptive prominences using the model of a partial current-carrying torus loop anchored to the photosphere. Based on these calculations, they concluded that the gravity force could be the most suitable agent to stop the filament eruption. On the other hand, based on simulations, the articles by Fan and Gibson (2003), Amari et al. (2018) propose a simple solution, i.e. a flux rope and embedded filament do not erupt because of the overlying field that Amari et al. (2018) call a magnetic cage.

In this article we present ground- and space-based observations (Section 2) of a sequence of events (Section 3) that ended with the failed eruption of a filament. The chain of events (filament formation, failed eruption, and associated flare) occurred on 9 May 2019 in the decaying AR 12740, where the main sunspot was surrounded by a moat region, as well as several small bipole emergences. Consequently, we observe locations of emerging and cancelling flux leading first to the filament formation (Section 3.2) and later to its eruption (Section 3.4). The eruption, which failed, was accompanied by a flare (Section 3.3) of C6.7 X-ray class recorded by the Geostationary Operational Environmental Satellite (GOES) starting at 05:40 UT, a maximum at 05:51 UT, and an extension of around two hours. Figure 1 shows AR 12740 in full-disk images at the time of the flare. We present local and global magnetic field models in Section 4 and, based on our modelling and observations, we propose a scenario to explain the observed events (Section 4.3). Finally, we summarise and conclude in Section 5.
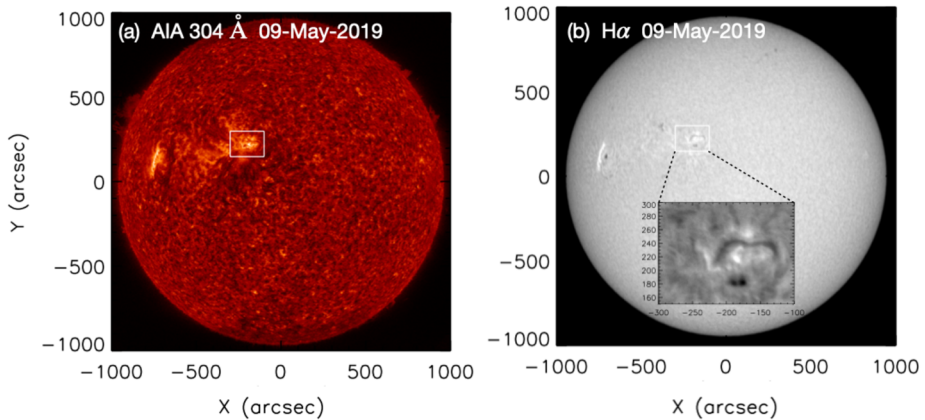
Figure 1 Full-disk images showing AR 12740 (*white box*) in: (a) AIA 304 Å band and (b) in GONG Learmonth Hα image on 9 May 2019 at 05:39 UT including a zoom on the filament. The *white box* in panel b covers the FOV of Figures 5 and 6.

2. The Data Used

To analyse the series of events that occurred in AR 12740 on 9 May 2019, we use extreme-ultraviolet (EUV) and ultraviolet (UV) data from the Atmospheric Imaging Assembly (AIA: Lemen et al., 2012), on board the Solar Dynamics Observatory (SDO), EUV observations from the Extreme Ultraviolet Imager (EUVI: Wuelser et al., 2004) of the Sun-Earth Connection Coronal and Heliospheric Investigation suite (SECCHI: Howard et al., 2008), on board the Solar-Terrestrial Relations Observatory (STEREO) spacecraft A and from the Interface Region Imaging Spectrograph (IRIS: De Pontieu et al., 2014). Hα data come from the Learmonth Solar Observatory (LSO) of the National Solar Observatory/Global Oscillation Network Group (NSO/GONG) and magnetograms from the Helioseismic and Magnetic Imager (HMI: Scherrer et al., 2012), on board SDO.

AIA provides full-disk images at seven EUV and two UV wavebands, with a pixel size of $0.6''$ and a cadence of 12 s and 24 s for EUV and UV, respectively. The higher-temperature wavebands, including 94 Å (6.3 MK), 131 Å (0.40 MK, 10 MK, 16 MK), 171 Å (0.63 MK), 193 Å (1.3 MK, 20 MK), 211 Å (2.0 MK) and 335 Å (2.5 MK), typically show features in the corona such as loops. The lower-temperature wavebands, 304 Å (0.050 MK), 1600 Å (0.10 MK) and 1700 Å (continuum) are sensitive to heating in the chromosphere. In our analysis we use the 304 Å, 171 Å and 1600 Å bands (henceforth, AIA 304, AIA 171 and AIA 1600). We select, from the full-disk images, sub-images containing the region of interest. The images are coaligned to compensate for solar rotation and the movies that accompany this article are constructed (Section 3.3). The images are either displayed in logarithmic intensity scale for better contrast or using the multi-scale Gaussian normalisation (MGN: Morgan and Druckmüller, 2014) processing technique.

We complement the SDO/AIA data with full-disk observations in the 304- and 195-Å channels of the STEREO-A/EUVI instrument (henceforth, EUVI-A 304 and EUVI-A 195). EUVI provides images with a pixel size of $1.6''$ and a temporal cadence of 10 minutes for EUVI-A 304 and 5 minutes for EUVI-A 195 during the analysed events. On 9 May 2019, the STEREO-A spacecraft was located at an Earth ecliptic (HEE) longitude of $-95°$; from this location AR 12740 was seen at the west solar limb.

IRIS observed AR 12740 between 04:54 UT and 06:21 UT in the mode of very dense rasters and, simultaneously, obtained slit-jaw images (SJIs) centred on the AR with a FOV of 167 × 175 in four channels around 1330 Å, 1400 Å, 2796 Å and 2832 Å, including C II, Si IV, Mg II lines and the UV continuum, respectively. C II is formed around T = 30 000 K and Si IV around 80 000 K, while Mg II is formed at chromospheric temperatures between 8000 K and 20 000 K. The cadence of the SJIs is 65 sec and the pixel size is 0.35″.

The Hα data come from LSO and have a spatial resolution of approximately 2″; they are obtained with a cadence of 1 minute. The analysed SDO/HMI data consist of line-of-sight (LOS) full-disk magnetograms (0.5″ pixel size) and synoptic maps. As was done for AIA, we select from the full-disk magnetograms sub-images centred in the AR and, after co-alignment, we construct the movies that are attached to this article (Section 3.1). The magnetograms are used to study the evolution of the AR magnetic field, as described in Section 3.1 (with 45 s cadence), and as boundary conditions for the local model described in Section 4.2 (720 s cadence). HMI synoptic maps are computed from LOS magnetograms by combining central meridian data from 20 magnetograms collected during a 4-hour interval each day. A synoptic map is made with the magnetograms observed over a full solar rotation with 3600 × 1440 steps in longitude and sine latitude. Details concerning the construction of synoptic maps can be found in the HMI web-site jsoc.stanford.edu/jsocwiki/SynopticMaps; the map for Carrington rotation (CR) 2217 is used as boundary condition for the model in Section 4.4.

3. The Events on 9 May 2019 in AR 12740

3.1. The Magnetic Field Evolution

AR 12740 appeared on the eastern solar limb on 4 May 2019. By the time of the events described in this article it was located at N10 E07. This AR is the return of AR 12738 on the previous CR. Figure 2 shows the magnetic field distribution on 12 April and 9 May 2019. On 12 April, AR 12738 consisted of a leading concentrated negative-polarity spot already in its decaying phase followed by a disperse positive polarity to the east. An extended moat region was present around the main negative polarity. Moat regions (see van Driel-Gesztelyi and Green, 2015, and references therein), which appear mostly around evolved and decaying spots play a key role in transporting flux away from spots and, therefore, contributing to their decay. Furthermore, moat regions are the sites of active phenomena, e.g. eruptions and recurrent jets (Chen et al., 2015; Chandra et al., 2015; Shen et al., 2018). The moat region around the strong negative spot in AR 12738 was also present one rotation later (compare both panels in Figure 2).

The evolution of the moat region is well visible in the panels presented in Figure 3 and the accompanying movie. This figure shows the leading negative spot (red oval) surrounded by a part of the moat region (yellow circle). The main spot decreases in size, while small magnetic features, called moving magnetic features (MMFs: Harvey and Harvey, 1973), move away from the spot (see arrows).

Besides this constant radial motion of the MMFs, we observe the emergence of several small bipoles toward the north of the main spot that made the full configuration highly dynamic (see the movie HMI_09May2019_Fig3.mp4). These series of emergences and their consequent evolution created a PIL nearly E–W oriented where a filament formed as discussed in Section 3.2.
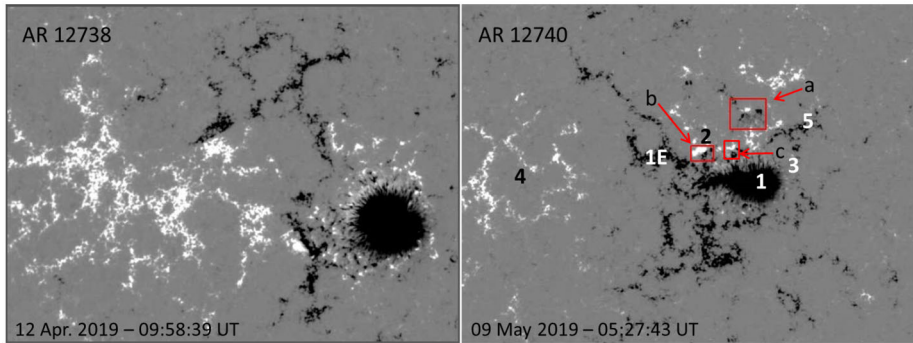
Figure 2 *Left panel*: Large-scale magnetic configuration of AR 12738 on April 2019 on CR 2216. A compact preceding negative spot, surrounded by a moat region, is followed by a disperse following positive polarity. *Right panel*: AR 12740, the return of AR 12738 on the next CR, showing a similar configuration. The *red rectangles* surround regions where we observe magnetic flux cancellation probably related to the events that occurred on 9 May 2019; they are indicated with *arrows* and labelled as a, b and c. Different magnetic polarities (or their extensions) that are relevant to our study are indicated with *numbers* (or a *number* and a *letter*). In both panels, *white (black)* regions correspond to positive (negative) LOS magnetic field measurements. The magnetic field values have been saturated above (below) 300 G (-300 G). The size of each panel is 330″ in the E–W (east–west) and 244″ in the N–S (north–south) direction. The centre of each panel in heliographic coordinates is N06 E07 for the *left panel* and N08 E01 for the *right panel*. A movie covering the evolution of AR 12740 from 7 to 9 May 2019 accompanies this figure (HMI_7-9May2019_Fig2.mp4); the magnetic field values have been saturated above (below) 500 G (-500 G) for a better visualisation of bipole emergences and changes during these days.
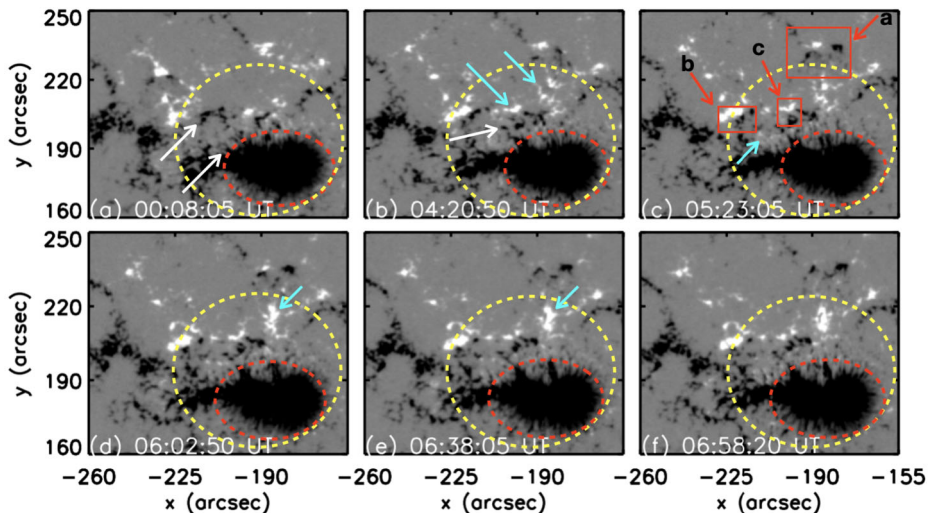

Figure 3 Evolution of part of the moat region surrounding the leading negative spot between 00:08:05 UT and 06:58:20 UT on 9 May 2019. *White/cyan arrows* indicate negative/positive MMFs rapidly changing. The *red oval* and the *yellow circle* have the same size in all the panels; this facilitates the visualisation of the contraction of the main negative polarity and the expansion of the region where MMFs are visible. In panel (c) red boxes a, b and c, similar to those in Figure 2, are drawn and indicated by *red arrows*. The magnetic field values have been saturated above (below) 400 G (−400 G). A movie with a similar FOV and of similar saturation accompanies this figure (HMI_09May2019_Fig3.mp4).
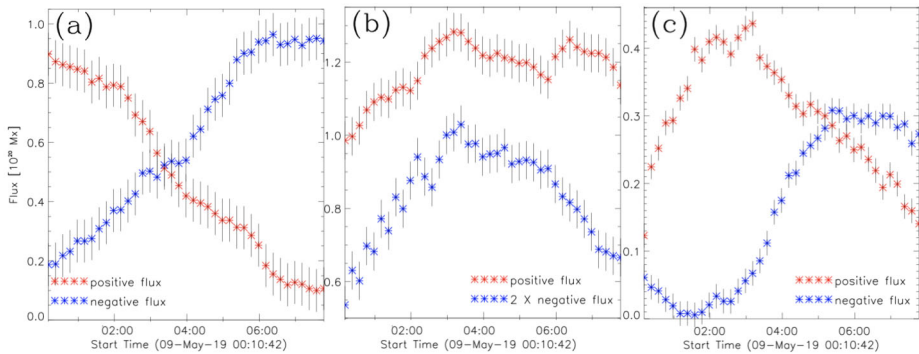
Figure 4 Evolution of the positive and absolute value of the negative magnetic fluxes in regions related to the filament formation and eruption. (a) Corresponds to the region within the *rectangle* labelled as a in Figure 2 where two long and wide fibrils merge to form the curved AR filament. Panels (b) and (c) show the flux evolution in regions labelled as b and c in Figure 2 that can be associated with the filament eruption. Note that in panel b the *blue asterisks* are multiplied by 2. Computations are done for values of the field above 10 G and the error bars are calculated considering a magnetic field error of 5 G.

We also identify several locations where flux cancellation occurred. Some of these are relevant to either the filament formation or its destabilisation, as discussed in Sections 3.2 and 3.4, *i.e.* see the rectangular boxes in Figure 2 (right panel) pointed with arrows and labelled as a, b and c. Figure 4 shows the evolution of the positive and negative magnetic fluxes within these boxes. Panel a corresponds to the region (labelled as a in Figure 2) where we identify the merging of two elongated and wide fibrils that finally formed a curved filament (see Figure 5 and Section 3.2); note that only the positive flux is seen decreasing, while the negative flux increases as it enters the southern boundary of this northern box. Panel b corresponds to the region (labelled as b in Figure 2) where we start observing the development of the two main ribbons of the C6.7 flare (see Section 3.3); note that in this case both negative and positive fluxes steadily decrease from around 03:10 UT until around 05:50 UT. Panel c shows the flux evolution in the rectangle (labelled as c in Figure 2). As in the case of region a, only the positive flux is seen decreasing after around 03:10 UT because negative flux, advected by the moat flow, enters the southern border of this rectangle. This region (c) could be related to the filament destabilisation (see the discussion in Section 3.3).

By the beginning of the flare and filament eruption (see Sections 3.3 and 3.4), the magnetic field distribution is the one depicted in the right panel of Figure 2. Since the magnetic configuration and its evolution is complex, we first limit its description to the quadrupolar configuration relevant for the studied flare and filament eruption. This involves polarities 1, 2, 3 and 4. Polarities 1 and 4 are the main ones of the AR. Polarity 2, which dramatically evolves in the hours previous to the flare, adds up to the quadrupolar layout. The fourth polarity that we call 3 is located to the west of polarity 1; following the evolution of the moat region around the main AR negative spot, this chain of polarities is formed by the MMFs moving away from the big spot.

In Figure 2, we have also labelled the extension of polarity 1, which ends at the border of a supergranular cell to the east, as 1E, as well as a north-western negative polarity that we call 5. This polarity is part of a bipole that emerged as early as 7 May 2019 at around 20:50 UT and evolved to the position shown in Figure 2 on 9 May; the positive bipole polarity is located to its north. Both 3 and 5 serve as a reference for our discussion in Section 4. A movie displays the complex evolution of AR 12740 from early 7 May to 9 May after the flare decay (HMI_7-9May2019_Fig2.mp4).
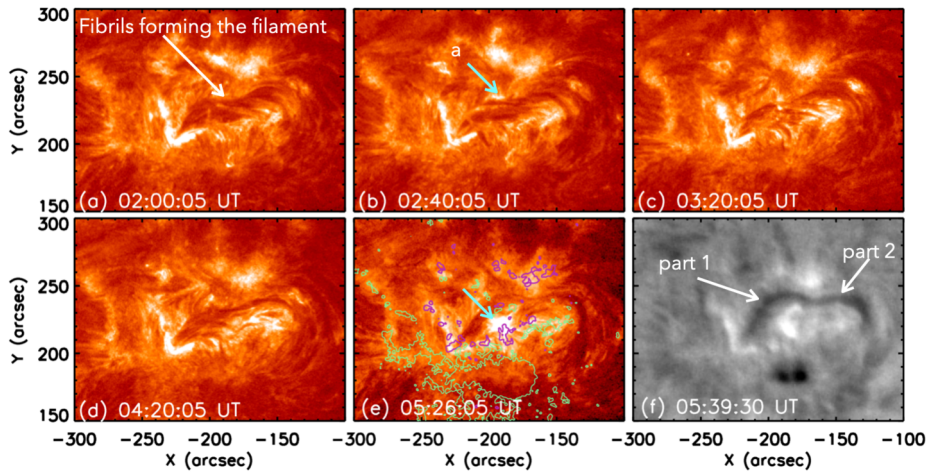
Figure 5 Formation of a long filament by the merging of fibril arcades to the N and W of the main sunspot in AR 12740 observed in AIA 304 (panels a–e) on 9 May 2019. Flux cancellation occurred in site a around 02:40 UT and continue (see *arrows* in panels a and b and the discussion in the text); this favoured the formation of a long curved structure. See text for the description of the evolution of this structure and the appearance of minor brightenings. A movie extending from 01:00 UT to 07:00 UT on 9 May accompanies this figure and Figure 6 (AIA304_09May2019_Fig3_Fig6.mp4). HMI contours of ± 100 Gauss (*magenta/green* for positive/negative polarities) are overlaid in panel e. Panel f presents Hα observations of the filament one minute before flare onset; its two parts are labelled as part 1 and part 2 and are indicated with *white arrows* (see text).

3.2. The Filament Formation

A long and curved filament started forming a few hours before the flare-initiation time at around 05:40 UT. Figure 5a shows sets of very long, wide and winding fibrils at 02:00 UT in AIA 304. Parts of these fibrils were involved in the merging process to form the long filament (Figure 5d). These fibril arcades evolved as time went on and seemed to merge at the location of magnetic flux cancellation; the white arrow in panel a points approximately to the magnetic flux cancellation site called a in Figure 2 (right panel), whose evolution is shown in Figure 4a. Panels b and c of Figure 5 depict this evolution. However, because the flux-cancellation process was accompanied by minor brightenings (see the light blue arrow in panel b), the elongated and curved filament structure appears interrupted by them, as can be better seen in panel c. We have called part 1 (labelled in Figure 5f) the eastern fibril arcade. Its negative polarity footpoints lie on the negative polarity at the flux-cancellation site a. Its other footpoints are anchored in the E–W branch of the positive polarity called 2 in Figure 2 (right panel). Note that polarity 2 has a global L-shape, with the longest part of the L in the N–S direction and the shortest in the E–W direction. Furthermore, by the time of all the panels in Figure 5 an L-shape plage brightening is seen tracing the polarity global shape. On the other hand, we have called part 2 (labelled in Figure 5f) the western fibril arcade with positive polarity footpoints at site a and negative footpoints most probably anchored in the disperse negative polarity 3 to the west of the leading spot (see Figure 2, right panel). By around 04:20 UT (see Figure 5d), the filament appeared as a single elongated and curved structure following the complex PIL created by the dynamics of the constant shuffling of the MMFs. However, by around 05:26 UT (see Figure 5e), the filament appears again as separated into two parts because of a brightening associated with the flux-cancellation site called c in Figure 2 (right panel). When seen in a high-time resolution movie in AIA 304,

this bright kernel marked by a light blue arrow in Figure 5e, corresponds to a small and localised jet and is not associated with the main C6.7 flare. Later, by 05:39 UT, one minute before flare onset in GOES, the filament is seen as a long curved structure in Hα (see panel f).

In summary, the filament is associated with opposite polarities converging and cancelling. This builds up progressively a coherent structure. Our observations agree and add to previous studies. Indeed, the evolution of fibrils merging and forming a filament has been already observed in cases where a filament formed from a loop arcade (see, e.g. Guo et al., 2010). Furthermore, the basic process of flux cancellation at fibril footpoints creating long magnetic field lines is also well described by van Ballegooijen and Martens (1989) and Schmieder et al. (2004). Filament formation from magnetic reconnection between adjacent short filament threads was observed and analysed in EUV and Hα observations (Yang et al., 2016; Xue et al., 2017; Chen et al., 2018). This kind of merging of short threads or fibrils through magnetic reconnection can originate bi-directional jets along the newly formed structure (Tian et al., 2017; Shen et al., 2017). We also observe these jets in an IRIS spectrum movie of our case study; however, it is out of the scope of this article to analyse IRIS spectra, we just add that bi-directional jets found in IRIS SJIs and spectra are well discussed in previous articles (Ruan et al., 2019; Joshi et al., 2021).

3.3. The Flare and its Multiple Ribbons

The evolution of the C6.7 flare is shown in three AIA wavelength ranges (AIA 1600 Å, AIA 304 Å and AIA 171 Å) in Figure 6 and in IRIS 1330-Å channel SJIs (Figure 7); note that AIA images depict a larger FOV than that of IRIS. Two movies with different temporal and spatial extensions accompany the figures in this section, AIA304_09May2019_Fig3_Fig6.mp4 and IRIS_CII_09May2019_Fig7.mp4. In both, despite the saturation in several images, the evolution of the flare and filament eruption at all of their stages can be followed.

Before describing the flare temporal evolution, we define the labelling of the distinctly observed flare ribbons in Figures 6 and 7 to facilitate our following description. This C6.7 flare consists mainly of a two-ribbon flare that occurred within the large quadrupolar magnetic configuration of the AR (see Figure 2 right panel). The double ribbons of the two-ribbon flare are called 2R (for two-ribbon flare) followed by a number that corresponds to the polarity number where the ribbon is located, as shown in Figure 2. We have also identified two additional ribbons, R3 located on the western and disperse negative polarity R3 and R4 located on polarity 4. These two ribbons are visible in Figures 6 and 7 and in the larger Hα FOV in Figure 9.

By around 05:43 UT the L-shape brightening, described in Section 3.2, is the most evident feature in the three AIA bands (see Figure 6), from chromospheric to low coronal temperatures. The evolution of the two-ribbon flare starts along the E–W extension of this brightening. The separation of its main bands is clear and increasing as in a typical two-ribbon flare in panels c, d, g and h of Figure 6 of both AIA 1600 and AIA 304. The relative shift of these two ribbons along the PIL indicates the presence of high magnetic shear at that location. Concerning IRIS, we focus on the C II band pass SJIs, in this band the two main ribbons are observed already at 05:43 UT in Figure 7a because IRIS SJIs have higher spatial and spectral resolution than AIA images, though a smaller FOV. Their evolution and separation is clearer than in Figure 6.

By around 05:49 UT, a ribbon that we label as R3 in panels c and g of Figure 6 is present to the west of the FOV on polarity 3. Simultaneously, another very elongated brightening is clearly seen to the east in Figures 6g and h, we have labelled it as R4. In the higher
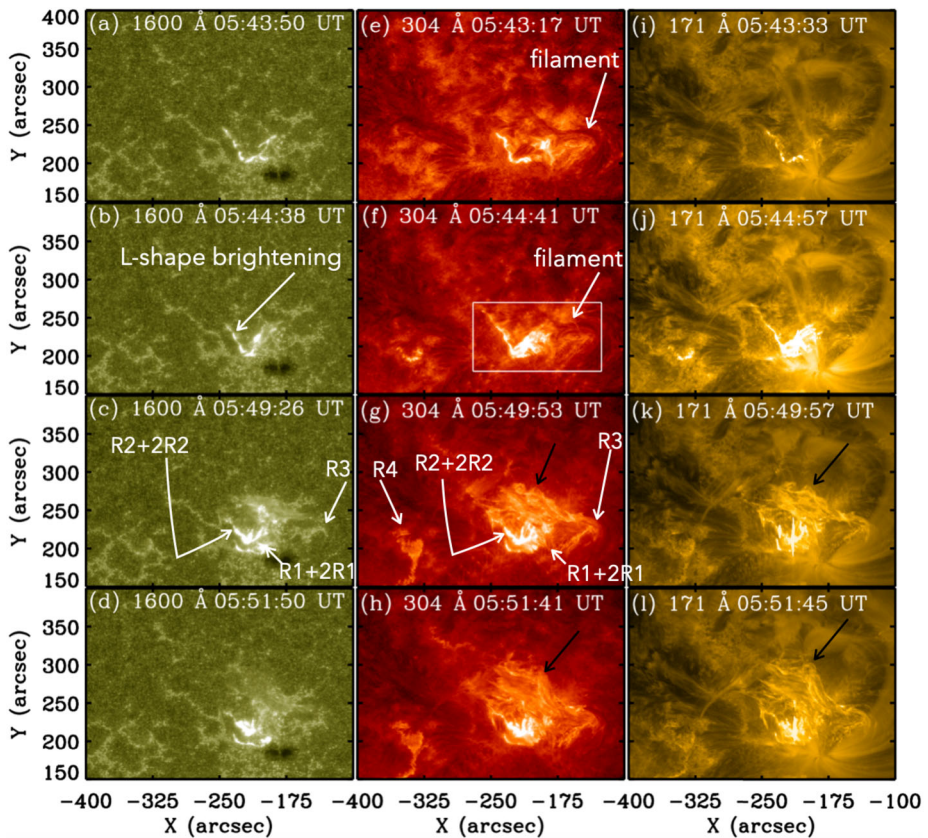
Figure 6 Evolution of the flare and the filament eruption in AR 12740 observed on 9 May 2019. The *left column* corresponds to AIA 1600, the *middle column* to AIA 304 and the *right column* to AIA 171. The *box* in panel f indicates the FOV of IRIS. The main flare ribbons visible in AIA 1600 are indicated with *arrows* in panel c and in AIA 304 in panel g. The western portion of the filament, which erupted a few minutes after the eastern portion, is indicated with an *arrow* in panels e and f of AIA 304 images. *Black arrows* in panels g, h, k and l indicate the northern edge of the heated filament plasma as it erupts. See text for the description of this figure and the movie AIA304_09May2019_Fig3_Fig6.mp4.

temperature AIA band, AIA 171, the northern portion of R4 appears in Figure 6j and its shape can be guessed in panels k and l. In a similar way as with the main ribbons 2R1 and 2R2, R3 is better seen in Figures 7c and d; however, R4 is not visible because of the reduced IRIS FOV.

Based on the appearance of the distant ribbons, R3 and R4, and our magnetic field model in Section 4.2, we conclude that the counterparts of R3 and R4 should be located on polarities 1 and 2, but we are not able to separate them clearly from 2R1 and 2R2. That is why we have labelled the extended ribbons along polarities 1 and 2 as R1+2R1 and R2+2R2 (see Figures 6 and 7) to indicate that they are possibly a combination of the main ribbons of the two-ribbon flare and the counterparts of R3 and R4 within the quadrupolar AR configuration.

Another feature, better seen at ≈ 05:47 UT in Figure 7d, is a curved brightening to the north of R3. This brightening is located on polarity 5 and the field-line connectivity derived in Section 4.2 allows us to conclude that it is not related to the C6.7 flare.
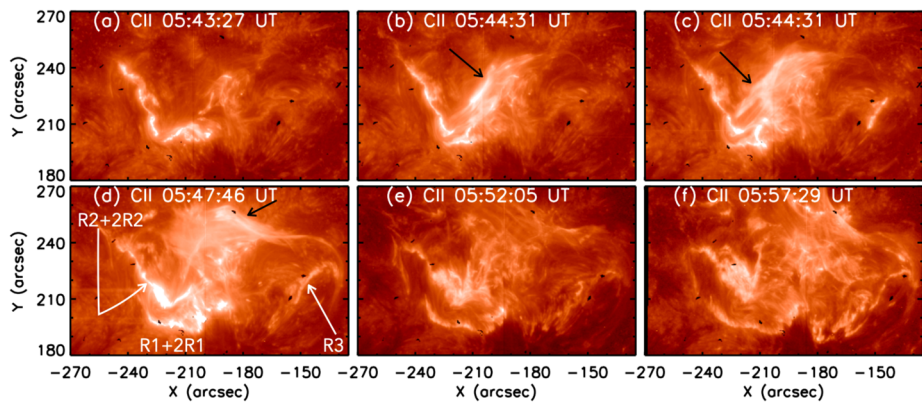
Figure 7 Evolution of the flare and filament eruption observed with IRIS 1330 Å channel between 05:43:27 UT and 05:57:29 UT. The main flare ribbons are indicated with *white arrows* and labelled in panel d. The evolution of the rising filament is indicated by *black arrows* in panels b, c and d. The up-going heated plasma of the filament is indicated with an *arrow* in panel d, as well as the western flare ribbon R3 that is also visible at this time. This FOV is indicated in Figure 6f. See text for the description of this figure and the accompanying movie IRIS_CII_09May2019_Fig7.mp4.

3.4. Failed Eruption of the Filament

In this section we describe the different observed stages of the filament eruption, from its lift off to the return of its plasma after its eruption has failed. We first discuss the observations as seen at the solar limb by EUVI in STEREO-A because from them, we can derive the ejection direction to help understanding the eruption as seen from Earth's perspective.

3.4.1. The Failed Eruption from STEREO-A Point of View

At the time of the event, STEREO-A was at a privileged location to observe the coronal activity related to AR 12740. From the STEREO-A point of view, AR 12740 appeared on its western solar limb, as shown in Figure 8. The panels of this figure correspond to EUVI-A 304 and 195 at different times from a few minutes after the beginning of the flare, when it is clearly seen on the limb of STEREO-A, and cover the filament eruption and consequent observation of plasma downflows. In this figure pairs of panels at similar hours are shown side by side for both channels. The images in these panels are shown in a grey-reversed scale and have been processed using a wavelet transform (see Stenborg, Vourlidas, and Howard, 2008). We point the reader to the movies that can be generated at cdaw.gsfc.nasa.gov/stereo/daily_movies/ not only showing the EUVI-A low corona but also the white-light corona as imaged by COR1-A and COR2-A.

The vantage point of view of STEREO-A provides information on the failed eruption, which is inaccessible from Earth's line of sight. We have used EUVI-A 304 and 195 images to compute the angles that the N–S and radial directions made with the average direction of the upflowing plasma. These angles are estimated from the pair of panels at the top right in Figure 8, where the average direction of the plasma upflow is shown with a red solid line and the radial and the N–S directions with blue ones. The dashed red lines indicate the plasma ejection width as projected on the plane-of-the-sky. The measured angles are almost
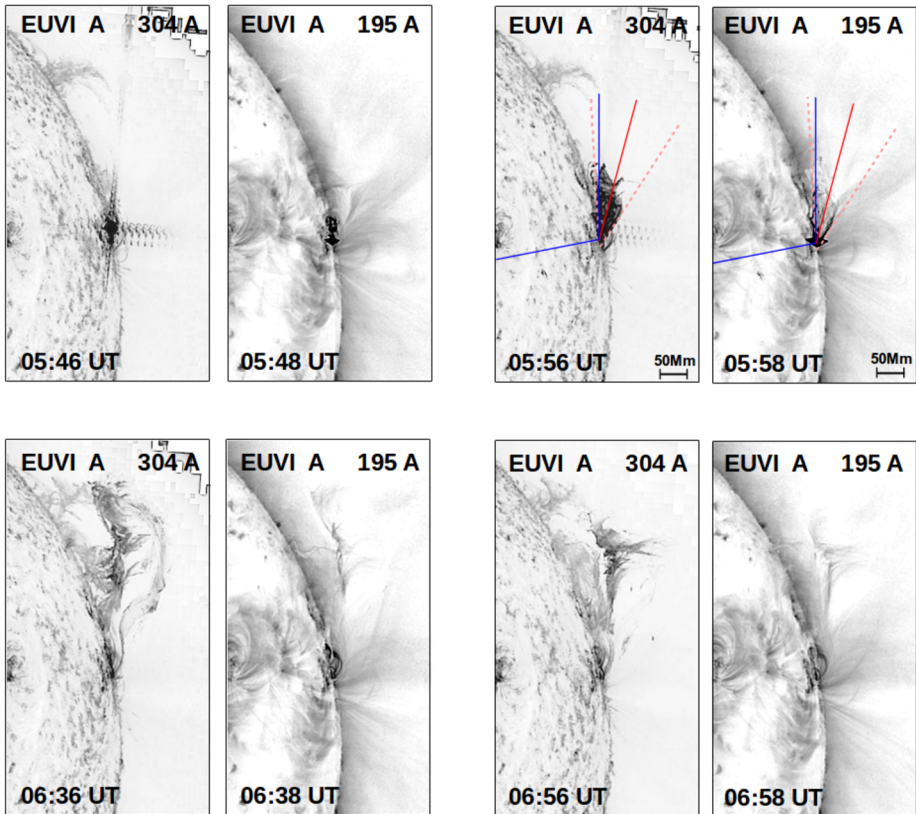
Figure 8 STEREO-A/EUVI images of AR 12740 in the 304 and 195-Å channels shown side by side at close-in-time hours. The spacecraft was approximately located on the ecliptic at an Earth ecliptic (HEE) longitude of −95° and the AR is observed on the solar limb. The saturated pixels (*in black*) correspond to the flare. The average direction of the mean prominence/plasma motion (*red*), the radial direction (*blue*), and the N–S direction (*blue*) are marked with *solid lines* in the top-right pair of panels. In the same panels, the *dashed red* lines indicate the plasma ejection width projected in the plane-of-the-sky. A *segment* has been added to the bottom right to indicate the figure scale size. The observation times are provided at the bottom left of each panel.

the same for both channels: $\approx 15°$ and $\approx 60°$ with respect to the N–S and radial directions, respectively. These values can be used to correct those of variables computed using data obtained from Earth's point of view (see Section 3.4.2 and Section 4.4).

We observed a CME whose leading edge appeared in STEREO-A COR1 FOV at 05:55 UT. However, we could not identify the CME source region in AIA images. Furthermore, the probable CME launch time, considering its projected speed in COR1-A images, would be before the start of the C6.7 flare. Therefore, we conclude that this CME is not related to the filament eruption we study (see Appendix).

3.4.2. The Failed Eruption from Earth's Point of View

In this section we discuss the different stages of the filament eruption as seen from Earth. We refer to the previously described Figures 6 and 7, stressing the aspects relevant to the
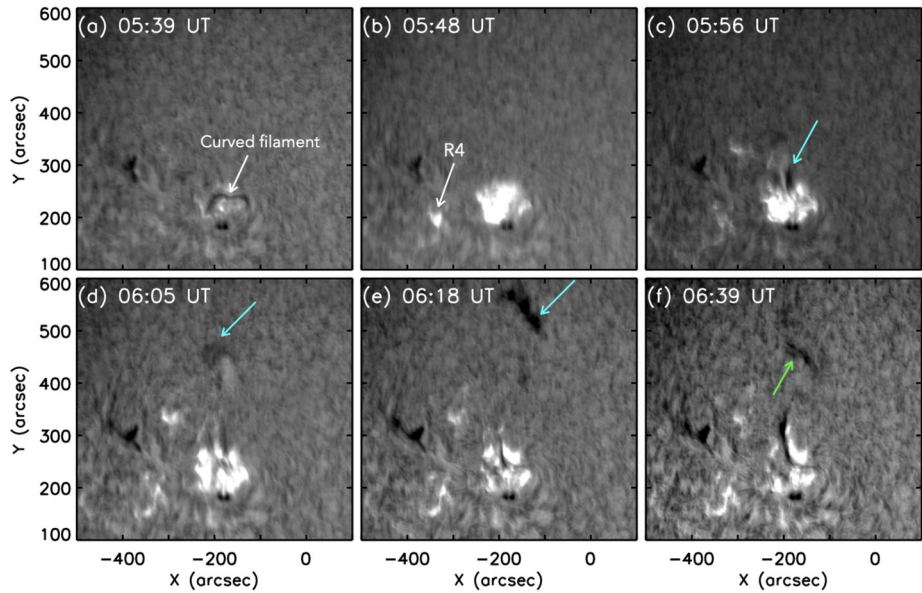
Figure 9 Evolution of the eruption in Hα observations stressing mainly its later stages. The curved filament before the eruption is well visible in panel a. In panel b we have labelled as R4 the elongated ribbon with a top rounded shape identified in AIA images (Figure 6). The cool material going upward is indicated with *light blue arrows* in panels c–e and with a *green arrow* when it is falling back in panel f. See the accompanying movie (Halpha_09May2019_Fig8.mp4).

eruption (see also movies AIA304_09May2019_Fig3_Fig6.mp4 and IRIS_CII_09May2019_Fig7.mp4). To these figures, we add Figures 9 and 10 that depict a larger FOV.

In Section 3.3 we have shown the existence of the two ribbons related to the C6.7 flare located in the centre of the active region, respectively, R1+2R1 and R2+2R2. The latter is the L-shape ribbon well visible in Figure 7d at 05:47 UT. Before this time, we already observe the lift off of part 1 of the filament, as indicated by the black arrow in Figure 7b. In the movie of IRIS we observe that this brightening becomes more diffuse and extends. Around 05:47 UT part 2 of the filament escapes. To the north of the two ribbons, we clearly see a large diffuse area with a bright northern edge oriented NE–SW (black arrow in Figure 7d). This large diffuse area is also visible later at 05:49 UT in AIA 304 Å (Figure 6g). As part 2 lifts, the whole filament appears as a large flux rope with a NE–SW orientation after 05:49 UT (black arrows in Figures 6g, k, h and l).

The evolution just described, as well as the location of the two main ribbons, described in Section 3.3, allows us to speculate that probably magnetic flux cancellation at sites b and c (see Figures 2 and 3 and Section 3.1) may have played a role in the filament destabilisation and eruption. In the higher-temperature AIA band, AIA 171, the most evident feature is the presence of the heated plasma extending upward in Figures 6j, k and l; note that part of the filament plasma seems to be flowing back already at around 05:51 UT.

We can continue observing the journey of the erupting plasma in Hα and AIA 171 in a larger FOV in Figures 9 and 10, and the corresponding movies after 06:00 UT until ≈ 06:20 UT. The AR viewed in AIA 171 is covered by a bright area of loops and straight features to its north (see white and green arrows in Figures 10b and c). The Hα material is seen to
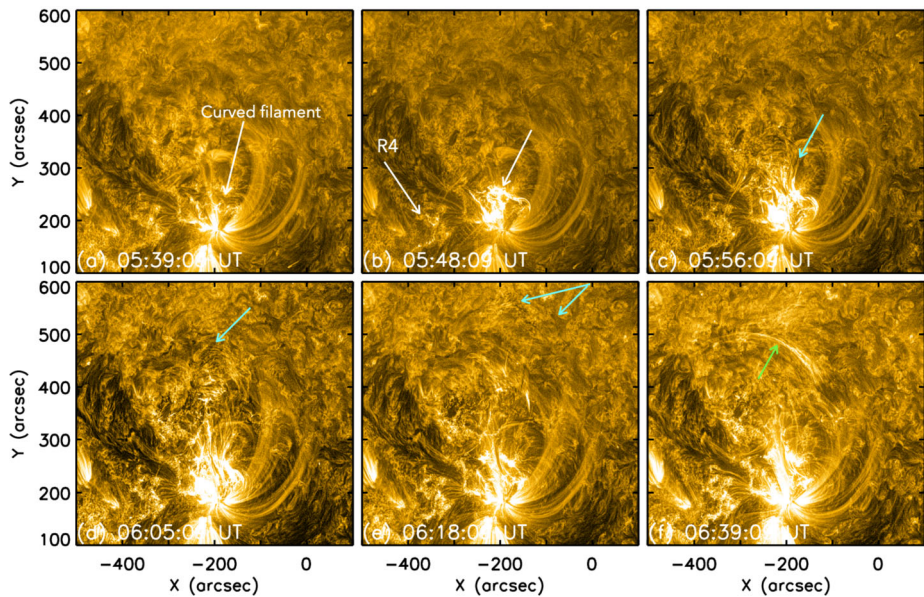
Figure 10 Evolution of the eruption in AIA 171 stressing mainly its later stages. Part of the curved filament before eruption is indicated with a *white arrow* in panel a. The elongated ribbon R4, as well as the up-going material, appear in panel b as indicated by the *white arrows*. Panels c, d and e show parts of the cool material going upward embedded in hot plasma (see the *cyan arrows*). Plasma falling back towards the solar surface after reaching its maximum height is indicated with a *green arrow* in panel f. The data are processed using the MGN technique for the better visibility. See the accompanying movie AIAMGN171_09May2019_Fig9.mp4.

move upwards in Figures 9d and e. However, simultaneously, the plasma is also observed falling down, dark in Hα and bright in AIA 171 in both panels f of Figure 9 and Figure 10. The falling-down material is progressively stack along large-scale loops, mostly visible in AIA 171 until 06:39 UT (Figure 10f).

To evaluate the speed of the rising and falling plasma we have built a stack plot along the N–S line that is shown in Figure 11a. Since the eruption of the filament, as well as the falling back of the plasma, is complex and appears to occur at different stages and along different directions, we have chosen only one direction that roughly agrees with the central location of the filament part 1 to have average speed estimations. Using the slopes of the white dashed line, drawn by hand in Figure 11b, which follows the leading edge of the material along the N–S line in panel a, we estimate a speed projected on the plane-of-the-sky of $190 \, \text{km} \, \text{s}^{-1}$ for the upflow and $60 \, \text{km} \, \text{s}^{-1}$ for the downflow. We deproject these values in the direction of the eruption using the angles measured in EUVI-A 304 and 195 in Section 3.4.1; when doing so, we obtain $201 \, \text{km} \, \text{s}^{-1}$ and $62 \, \text{km} \, \text{s}^{-1}$, respectively. These values are quite similar to those found on the plane-of-the-sky because of the very small angle between the directions N–S and that of the eruption. We also measure the distance reached by the plasma along the N–S direction, computed from around $70''$ in Figure 11b where the intense flare emission is seen in AIA 171, and find a value of ≈ 270 Mm; this corresponds to a distance of ≈ 280 Mm along the plasma-ejection direction (assumed to be along a straight line).
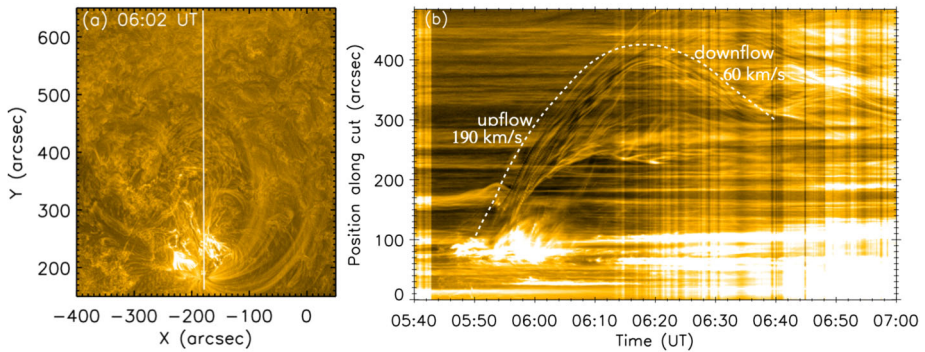
Figure 11 Height–time analysis of the filament eruption in AIA 171. The upward and downward projected motion of the plasma is measured along the N–S white slit in panel a on the AIA 171 image. The slit for constructing the stack plot is chosen manually by eye and roughly agrees with the central location of the filament part 1. Panel b corresponds to a stack plot built along the slit. For a better visibility of the upward- and downward-moving material, we have used the MGN technique to process the images used to build this plot. The *white dashed line* in this panel is drawn manually, following the leading edge of the material moving first upward and later downward.

4. Coronal Field Model of the Events on 9 May 2019

4.1. Overview

Following our multi-wavelength analysis of the phenomena in AR 12740 on 9 May 2019, we present in Section 4.2 a flare model of the magnetic field configuration at the AR scale size. The field line connectivity derived from this model allows us to propose a possible physical scenario (Section 4.3) and interpretation of the complex chain of events we have analysed. This section is followed by a global magnetic field model (Section 4.4) that complements and supports our proposed scenario and interpretation.

4.2. Local Magnetic Field Model

To understand the role of the different magnetic polarities in AR 12740, we model its coronal field. We extrapolate the HMI LOS magnetic field to the corona using the discrete fast Fourier transform method described by Alissandrakis (1981), under the linear force-free field (LFFF) approach ($\nabla \times \boldsymbol{B} = \alpha \boldsymbol{B}$, with α constant). Although this kind of modelling cannot take into account the distribution of currents at the photospheric level and the strong shear that we can infer from the shape and location of the ribbons of the two-ribbon flare, but only the shear in the global magnetic configuration, its computation is fast and has proven to be efficient to determine the magnetic field structure at the scale size of an AR, which can be later compared with observed active events (see, e.g. Mandrini et al., 2006, 2014, and references therein).

Figure 12 right panel shows an AIA 171 image before the flare (05:24:34 UT) in which large-scale magnetic loops are visible. Figure 12 left panel displays a set of blue field lines derived from the coronal model overlaid on the same AIA image. In this and all other coronal-field models, we use as boundary condition, the HMI magnetogram closest in time and we also apply a transformation of coordinates from the local frame, in which the computations are done, to the observed frame so that our models can be directly compared to
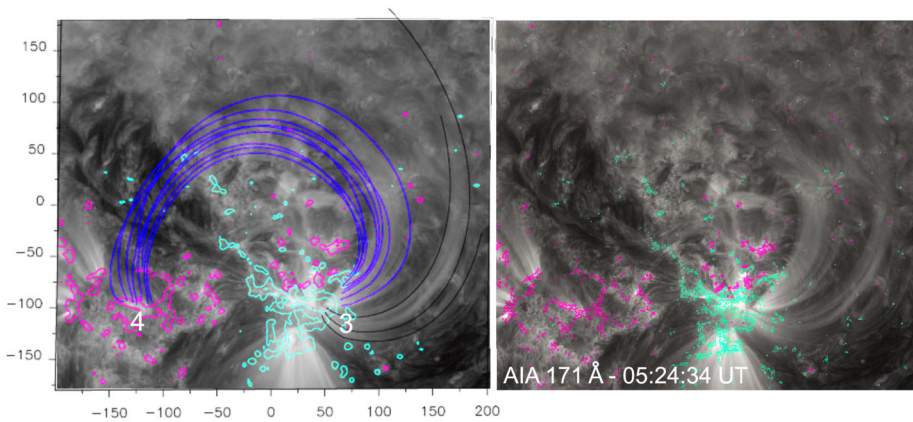
Figure 12 *Left panel*: Magnetic field model of the large-scale coronal loops connecting the chain of small negative polarities labelled as 3 to the disperse positive following AR polarity 4 (see Figure 2). A set of computed field lines in *blue solid traces* is overlaid on the AIA 171 image at 05:24:34 UT, together with HMI magnetic field contours ($\pm$ 100, 500 G, positive (negative) shown in *magenta (blue)* colour). The three *black field lines* connect to northern positive quiet-Sun regions out of the AR (compare to Figure 16). The axes in this panel are in Mm, with the origin set at the AR centre. *Right panel*: The same AIA image shown as background in the left panel for comparison. The image is shown in logarithmic direct intensity and we have added HMI isocontours of similar values to those in the left panel as a reference. The images are shown in *grey scale* to facilitate the visualisation of computed field lines and magnetic field contours in this figure and the following two.

the data (see the Appendix in Démoulin et al., 1997). The value of α, the free parameter of the model, is set to best match these large-scale loops (as discussed in Green et al., 2002). The best-matching value is $\alpha = 9.4 \times 10^{-3}$ Mm^{-1}. This large-scale loops are also present several hours after the flare has ended, as can be seen in images displayed in Helioviewer (helioviewer.org/), which means that the large-scale configuration persists.

Figure 13 right panel depicts an AIA 304 image 3 minutes before flare maximum (05:48:29 UT). The flare ribbons corresponding to the two-ribbon flare as those associated with the quadrupolar configuration have been labelled as indicated in Section 3.3. Figure 13 left panel displays a set of red field lines derived from the coronal model overlaid on the same AIA image. Since no flare loop is observed to compare with our computed field lines, the value of α is set so that the computed field lines connect the observed ribbons. The best-connecting value is higher than in Figure 12, $\alpha = 1.6 \times 10^{-2}$ Mm^{-1} and double this value for the sets of lines to the East and West, respectively. See the caption to this figure for an explanation of the set of black lines.

Finally, we model the loops observed during the flare-decay phase that are observed between the two main flare ribbons. Figure 14 right panel depicts an AIA 171 image at 06:04:21 UT, where the so-called post-flare loops are clearly seen. Figure 14 left panel displays a set of red field lines overlaid on the same AIA image that match the shape of these post-flare loops. The value of α that gives the best match is $\alpha = 1.6 \times 10^{-2}$ Mm^{-1}.

4.3. The Stages of the Observed Events

The results of the three just described models, together with our data analysis, leads us to the following conclusions about the origin of the C6.7 flare and its evolution. The connectivity determined from each model provides only a static view at the time it is computed; therefore,
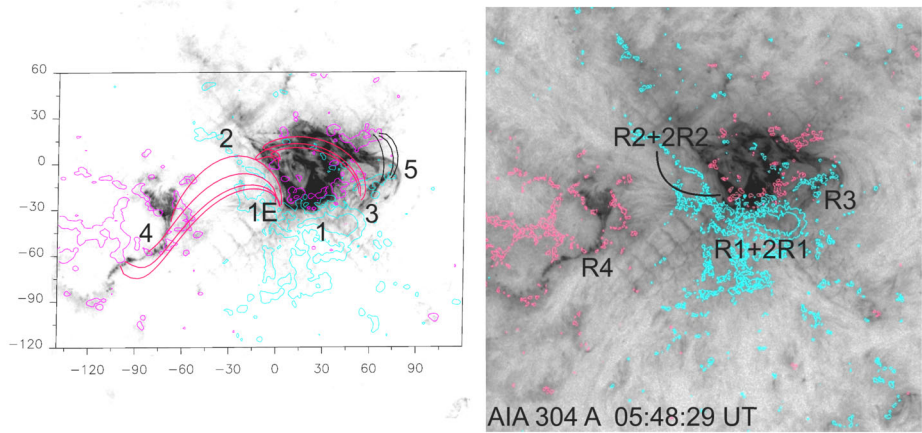
Figure 13 *Left panel*: Magnetic field model at the flare time. Sets of field lines in *continuous tracings* are overlaid on the AIA 304 image at 05:48:29 UT. The set in *red* to the east (west) connects the ribbon on polarity 4 (3) to the one on polarity 1 (2) and is the result of the external reconnection process discussed in the text (see Section 4.3). The set in *black* has been added to show that the negative polarity 5 (see Figure 2), where a curved brightening to the north of R3 is located, is connected to a northern positive polarity. The convention for HMI contours and axes are the same as in Figure 12. *Right panel*: The same AIA image shown as background in the left panel in logarithmic reverse intensity including HMI contours for reference, note the diffraction pattern because of the high flare intensity. The two-ribbon flare, 2R1 and 2R2 on polarities 1 and 2, and the ribbons of the quadrupolar external reconnection have been labelled in this panel. R1 and R2 are located on polarities 1 and 2 and, as discussed in the text, they cannot be clearly separated from the two main flare ribbons. Ribbon R3 is located on the chain of small negative polarities 3 and the extended ribbon R4 is located on 4.
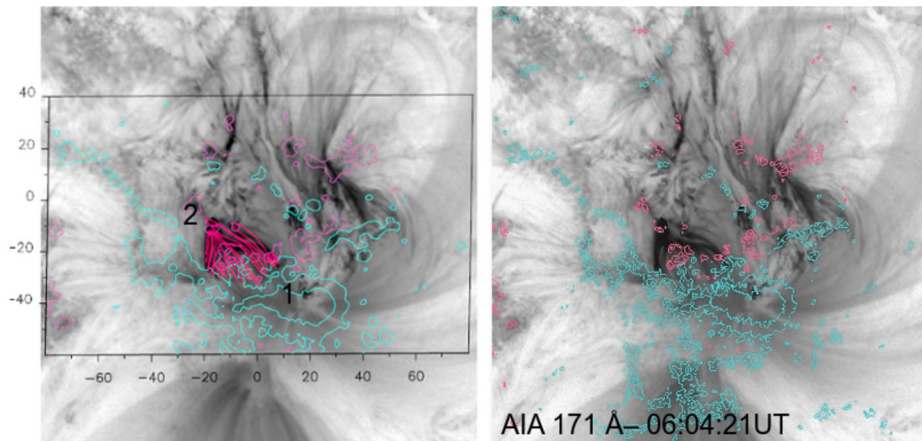
Figure 14 *Left panel*: Magnetic field model during the flare decay phase. A set of computed field lines in *red continuous tracing red solid traces* is overlaid on the AIA 171 image at 06:04:21 UT. This set corresponds to the loops connecting the two flare main ribbons and results from the internal reconnection process discussed in the text. The field lines are anchored to polarities 1 and 2. The conventions for HMI contours and axes are the same as in Figure 12. *Right panel*: The same AIA image shown as background in the left panel for comparison including HMI contours and using the same convention as in Figure 13. Note that some loops can be discerned between polarity 3 and a northern positive polarity as expected from the *black lines* added to Figure 13.
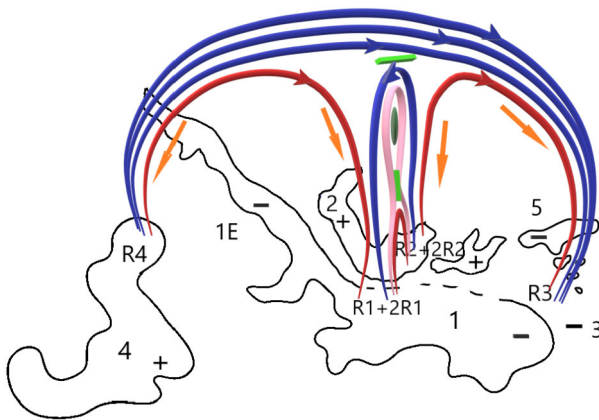
Figure 15 Sketch showing sets of field lines connecting several of the polarities identified in Figure 2. The relative locations and shapes of these polarities have been drawn and the sites of the different ribbons are indicated using the labels in Figure 13. The flux-rope configuration including the filament is simplified to a 2D representation. As the filament (indicated by a *green ellipse*) and its magnetic configuration rise two reconnection processes occur, as identified with *thick green segments*: the internal one below the filament and the external one above it. The former process gives the observed two main flare ribbons (2R1 and 2R2) located close to the base of the *pink line* and joined by a *red* reconnected field line. The latter process reconnects blue field lines (connecting regions on polarities 3 and 4) with *blue* elongated field lines (connecting 1 and 2), which overlay the rising filament. This process eventually derives in the injection of filament material in field lines connecting 1 to 4 and 3 to 2, highlighted in red. This material is observed flowing down (see *orange arrows*) along them, pinpointing the filament failed eruption (see Section 4.3 for a more detailed description). At the footpoints of the *red lines* we observe ribbons R1 and R2, which cannot be clearly separated from the two main flare ribbons resulting from the internal reconnection process, and the farther ribbons R3 and R4.

to facilitate our discussion of the different stages of the events and the processes that occur, we include the scheme shown in Figure 15. This sketch is similar to the one proposed by López Fuentes et al. (2018) and Poisson et al. (2020) for a failed mini-filament eruption.

The situation depicted in Figure 15 corresponds to a time at which the magnetic configuration containing the filament, drawn as a green oval, was already destabilised and rising. Probably, magnetic flux cancellation occurring at sites b and c destabilises the filament magnetic configuration that starts erupting (see references in Section 1 about filament eruptions driven by flux cancellation). A set of field lines (anchored between 1 – 2) overlays the filament that is located along the main AR PIL (see the elongated blue line lying above the filament). The set of long blue field lines (anchored between 3 and 4, see Figure 12 left panel and Figure 15) corresponds to the closed background field.

Magnetic reconnection sets below the filament, as happens in a classical prominence eruption (see, e.g. Aulanier et al., 2010; Webb and Howard, 2012). The location of this reconnection process is represented by the green vertical segment in the sketch. The pink field line marks the limit between the reconnected field lines below the filament and those surrounding it. In our model, the red field lines in Figure 14 left panel correspond to the reconnected lines resulting from this process below this limiting pink line. The just described reconnection process has been called internal in several articles (see, e.g. Sterling et al., 2015; Moore, Sterling, and Panesar, 2018).

As the filament configuration moves up, field lines located above the filament (the blue elongated line in the sketch) start reconnecting with the large-scale blue lines shown in our model in Figure 12 left panel and outlined in blue in the sketch. This second recon-

nection process, indicated by the green oblique segment, has been called external in the just-mentioned references.

As a result of the external reconnection process, the filament plasma and that of the loops where it is still embedded, is injected into the red reconnected field lines. The material is seen flowing down along them (as indicated by the orange arrows in the sketch) and the eruption fails. The external reconnection process decreases the magnetic tension above the filament flux rope. However, if the large-scale magnetic field (in the blue arcade connecting 3 to 4) has more flux than that of the flux rope, the latter could be mostly reconnected and could not continue upward.

To investigate the latter statement, we first compute the magnetic flux swept by the ribbons of the two-ribbon flare using AIA 1600 images overlaid on the corresponding HMI magnetograms (the two ribbons are better seen and not saturated in this AIA band). The flux swept by the ribbons represents the flux added by reconnection to the erupting flux rope (see, e.g. Deng and Welsch, 2017, and references therein) and is a lower bound for the flux-rope total flux. This estimated average flux is $\approx 1.5 \times 10^{20}$ Mx for the time range $05:43 - 05:53$ UT (see AIA 1600 images in Figures 6a–d). As a second step, we compute the flux in the large-scale overlying arcade taking into account the region on polarity 4 that connects to polarity 3 in our local-field model (we use only polarity 4 because the counterpart region on polarity 3 is continuously evolving because of the shuffling of MMFs). The flux in the large-scale arcade is $\approx 8.5 \times 10^{20}$ Mx, ≈ 6 times larger than the flux-rope flux. This supports our assumption of a fully reconnected erupting flux rope. In addition to this, the kinetic energy of the filament with a speed of 183 km s^{-1} could be too small for a successful eruption, see, e.g. Shen, Liu, and Liu (2011) who studied three filament eruptions, two failed and one successful, and found that the filament velocity in the successful one was the largest and that filament velocities were proportional to the power of their flares.

In summary, the first internal reconnection process would result in the observed intense two ribbons labelled as 2R1 and 2R2 in Figures 13 (right panel) and 15. They are located at both sides of the PIL between polarities 1 and 2, and the very short post-flare loops joining them (see Figure 14 left panel). The second external reconnection process is associated with ribbons R4, R3 and their counterparts on polarities 1 and 2 that we have called R1 and R2 (Figures 13 right panel and 15). As already mentioned, these ribbons cannot be clearly separated from the main two flare ribbons and we only have an idea of their location based on the field-line connectivity computed from our model shown in Figure 13 left panel. In the studied event, as stated above, the second external reconnection process is most relevant in impeding the filament flux-rope eruption.

4.4. Global Magnetic Field Model

Since our local-field model is limited to the scale size of the AR, we have computed a global coronal magnetic model to verify that the magnetic configuration at this larger scale remains closed.

The global coronal magnetic field of CR 2217 is modelled using a potential-field source-surface (PFSS) approach. These models assume a current-free coronal field with an observationally prescribed boundary condition at the photosphere. PFSS models assume that the field becomes purely radial at a given height, called the source surface, which in our case is set to a value of 2.5 $R_\odot$. Our PFSS model uses as its lower-boundary condition the corresponding HMI magnetic field synoptic map.

The model is carried out using the Finite Difference Iterative Potential-Field Solver (FDIPS) code described by Tóth, van der Holst, and Huang (2011). This code is freely
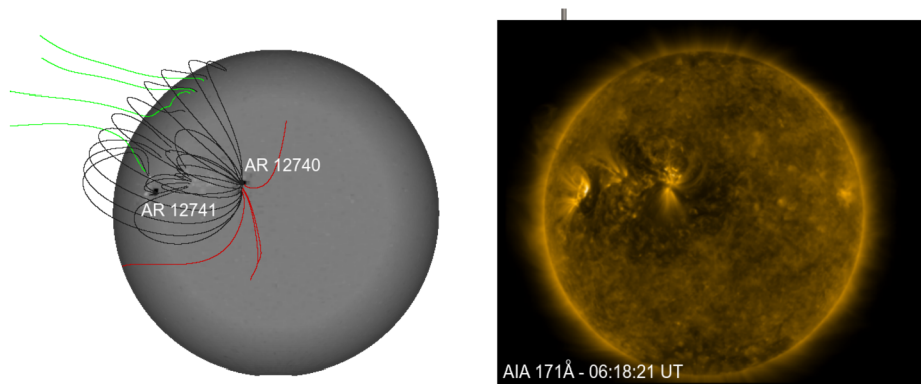
Figure 16 *Left panel*: PFSS model of CR 2217 with AR 12740 located at Carrington longitude 318° on 9 May 2019 close to the flare time. The field-line colour convention is such that *black* indicates closed lines and *pink (green)* corresponds to open lines belonging to the negative polarity (positive polarity) field (note that open implies reaching the source surface). Closed field lines connect the AR main negative sunspot to its following positive polarity as in the model in Figure 12. Note that the curvature of this set of closed field lines is different from the set shown in *blue* in that figure since this is a potential-field model, while the local-field model considers the shear at the AR scale-size. Other closed lines connect north to quiet-Sun regions as in Figure 12 (lines shown in *black*) or to the positive field of the trailing AR 12741. The magnetic field values have been smoothed and saturated above (below) 250 G (-250 G). *Right panel*: AIA 171 full-disk image as reference at the time corresponding to the Carrington longitude in the left panel.

available from the Center for Space Environment Modeling (CSEM) at the University of Michigan (csem.engin.umich.edu/tools/FDIPS). It uses an iterative finite-difference method to solve the Laplace equation for the magnetic field. In this particular case, the spatial resolution is 1° in longitude (360 longitudinal grid points), 0.011 in the sine of latitude (180 latitudinal grid points) and 0.01 $R_\odot$ in the radial direction.

Figure 16 left panel shows the result of our modelling together with a set of field lines computed starting integration at a height of 150 Mm in both directions. The integration points are located in AR 12740, its neighbourhood, and the trailing AR 12741. It is clear that the magnetic field configuration remains closed at the large scale, with closed lines connecting the leading and following AR polarities and also the leading negative polarity to quiet-Sun regions located far to the north of the AR. Figure 16 right panel shows an AIA 171 full-disk image as reference, the large-scale loops connecting both AR 12740 polarities are clearly seen.

We have computed the magnetic tension force or magnetic tension, $\boldsymbol{B} \cdot \nabla \boldsymbol{B}/\mu_0$, with $\boldsymbol{B}$ the three components of the magnetic field directly derived from the PFSS model and μ_0 the vacuum magnetic permeability), at different heights (Figure 17). The magnetic tension is directed towards the centre of curvature of the field lines and acts as a restoring force, which works against the ejected magnetic field. Figure 17a shows the HMI synoptic map for CR 2217 that helps us identify the locations of AR 12740 and the trailing AR 12741. Figure 17b shows that the magnetic tension force is the largest over both ARs compared to the surrounding. This is the case over a broad interval of heights (at least up to 500 Mm), while the prominence stays confined lower down (Figure 8). We also compute the magnetic tension force along the prominence trajectory, approximated by a straight line inclined to the local vertical as observed by STEREO A (Figure 8). Figure 17c shows the results for the trajectory located within three meridional planes. While the magnetic tension decreases rapidly along the trajectory, it stays large compared to the surroundings (panel b). Note that
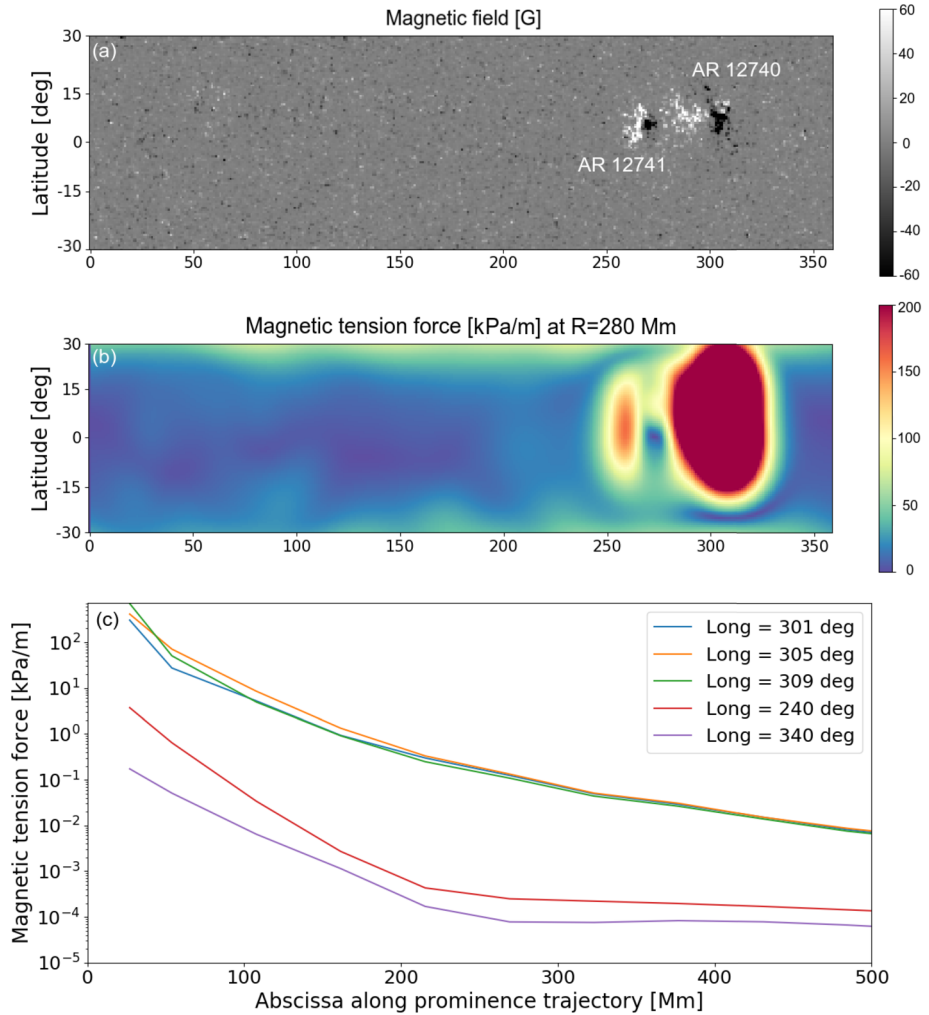
Figure 17 From top to bottom: (a) Synoptic HMI map of CR 2217. The horizontal axis indicates the Carrington longitude and the vertical axis on the left corresponds to the Carrington latitude. Note that we have limited the latitudinal extension to ± 35 deg to exclude field lines that are considered open in the PFSS model. A *greyscale bar* showing the magnetic field scale intensity has been added to the right. (b) Magnetic tension force at a height of 280 Mm, with the same coordinates than in (a). A *colour bar* showing the magnetic tension scale has been added to the right. (c) Magnetic tension force as a function of the coordinate along the prominence trajectory computed at three different longitude values at the AR location. The trajectory is assumed to be a straight line, inclined to the local vertical as observed (Figure 8) and set within a fixed meridian plane. We have also added two curves computed in a similar way at two different longitudes to the east and west of ARs 12741 and 12740 for comparison.

we have also added two curves computed in a similar way, but at both sides (*east and west*) of ARs 12741 and 12740, to stress the difference between the values of the tension in the surroundings from those in the AR where our events occurred. This allows us to conclude that it is the magnetic tension of the overlaying field that prevents the filament configuration erupting (see references in Section 1). Despite the fact that the magnetic tension can be

decreased by forced reconnection between the erupting magnetic field and the overlying arcade, the latter has enough magnetic flux and intensity to stop the filament eruption at a moderate height.

5. Summary and Conclusions

We analyse a series of events that occurred in AR 12740 on 9 May 2019 using a set of multi-wavelength observations going from the photosphere to the corona obtained by HMI, AIA, STEREO, IRIS and GONG/LSO instruments. The chain of events includes the formation of a filament, its destabilisation and the accompanying flare, followed by the filament failed eruption. Our study allows us to conclude on the origin of each of the different steps in this chain.

AR 12740 was in its decaying phase characterised by the presence of MMFs surrounding a compact and high-intensity field negative leading polarity followed by a very disperse positive one. Though the AR could be globally considered as bipolar, the constant advection of minor polarities from the main spot into the surrounding moat region and the emergence of small bipoles created a very complex and dynamic magnetic configuration. A detailed study of the magnetic field evolution leads us to identify four main polarities that played a key role during the filament eruption and flare, i.e. these two events occurred within a mainly quadrupolar AR (see Section 3.1). Magnetic flux cancellation within the moat region to the north of the main spot, in a site that we called a (see Sections 3.1 and 3.2), was the origin of the formation of a long and curved filament by reconnection between sets of fibrils, as in the model proposed by van Ballegooijen and Martens (1989) (see an observed example in Schmieder et al., 2004).

In a similar manner, magnetic flux cancellation was at the origin of the destabilisation of the flux rope containing the filament plasma (see Sections 3.1 and 3.4). This mechanism was proposed in several examples and simulations of mini-filament eruptions followed by blow-out jets (see reference in Section 1). The flux-cancellation process was mainly due to the constant shuffling of the MMFs at two different sites (sites b and c) by the PIL around the main spot. This eruption was accompanied by a two-ribbon flare whose main ribbons were located on the main negative polarity and an L-shape positive polarity to its NE (see Section 3.3). However, because the global magnetic configuration of AR 12740 was quadrupolar, two additional ribbons were seen far to the *east and west* of the two-ribbon flare. A force-free magnetic field model at the AR scale size allows us to connect the far flare ribbons between themselves and to the extensions of the two main flare ribbons, *i.e.* the flare was in fact a six-ribbon event confined by the larger-scale loops of the quadrupolar configuration (see Sections 4.2 and 4.3).

Even though the flux rope containing the filament erupted, this eruption failed, thus plasma was observed first moving upwards and later downwards. Based on our local magnetic field model, we propose a scenario (see Section 4.3) in which the failed eruption and multi-ribbon flare are the result of two reconnection processes, one occurring below the erupting flux rope, leading to the two-ribbon flare, and another one above it between the filament configuration and the large-scale closed loops of the quadrupolar configuration. This second process leads to the appearance of the far flare ribbons and their counterparts (as extensions of the main two ribbons). In a similar way, it injects plasma from the filament and the loops where it is embedded, within the reconnected loops linking the ribbons of the quadrupolar configuration. These two reconnection processes have been called internal and external in articles describing mini-filament eruptions (see, e.g. Sterling et al., 2015;

Moore, Sterling, and Panesar, 2018, and references therein). Furthermore, via this external reconnection process, the erupting flux rope could fully reconnect with the large-scale closed loops because, as we have shown, its magnetic flux is much lower. A PFSS model confirms that AR 12740 was confined by closed field lines connecting both AR main polarities and the main negative polarity to quiet-Sun regions. Additionally, from this model we compute the magnetic tension of the large-scale magnetic field at a height above that reached by the erupting plasma and conclude that above the AR it was much larger than in other locations on the Sun (see Section 4.4). Therefore, from the point of view of the global magnetic configuration, we also find hints that would lead to a failed filament eruption.

Summarising, from an observational point of view, this case study is clearly consistent with models proposing that filaments can be formed from converging fibrils at flux-cancellation sites, as well as destabilised by similar flux-cancellation processes (see references in Section 1). Furthermore, it represents a well-observed example of how magnetic confinement by an intense overlying field can lead to failed flux-rope eruptions, as proposed by several MHD simulations (e.g. Fan and Gibson, 2003; Amari et al., 2018).

Appendix: Study of the CME Visible by STEREO-A COR1

For completeness, we analyse a CME whose leading edge appears in the STEREO-A COR1 FOV at 05:55 UT, which we briefly describe here. We also refer the reader to the movies that can be generated at cdaw.gsfc.nasa.gov/stereo/daily_movies/ for a quick look at the CME event. Its projected speed at the central position angle as measured in COR1-A images yields 246 $\mathrm{km\,s^{-1}}$. When reaching the COR2-A FOV, the CME appears faint and diffuse, but is nonetheless detected by the Solar Eruption Detection System (SEEDS, spaceweather.gmu.edu/seeds/monthly.php?a=2019&b=05&cor2) at George Mason University. In this data base, the CME position angle is 260°, *i.e.* 10° south from the solar equator, and its speed in the plane-of-the-sky is 233 $\mathrm{km\,s^{-1}}$, in good agreement with the value we compute from COR1-A images.

Although it is out of the scope of our work, we attempted, unsuccessfully, to identify the CME source region in AIA images, as well as in the Hα ones from LSO. Further inspection, now from the quadrature vantage point provided by STEREO-A, shows coronal material at a fairly high altitude ($\sim 1.4\,R_\odot$) and at a position angle of $\approx 285°$, that starts moving outward in a radial fashion, apparently destabilised and triggered by the flare we study. Given this scenario, we speculate that we are dealing with a stealth event, originating due to the destabilisation of a barely visible structure that lies at a significant height above the solar surface, already prior to the start of the C6.7 flare. Whether this CME eruption magnetically connected to the failed eruption or not, both can be regarded as separate events due to a number of reasons. First, and as mentioned above and shown in Figure 8, the failed eruption moves with an angle of $\approx 60°$ with respect to the radial direction, whilst the outward-travelling coronal material seen at a high altitude propagates nearly radially. Secondly, the failed filament eruption is seen to turn back at $\sim 06:30$ UT, while the CME at that time is at $\approx 3\,R_\odot$ and reaches the COR2-A FOV at 06:54 UT. Therefore, because of timing and the propagation direction, compared to that of the filament failed eruption seen in EUVI-A images, we conclude that the CME observed in COR1-A and COR2-A can be regarded as not affecting the events analysed in this article.

Declarations

References

Alissandrakis, C.E.: 1981, On the computation of constant alpha force-free magnetic field. *Astron. Astrophys.* **100**, 197. ADS.

Amari, T., Canou, A., Aly, J.-J., Delyon, F., Alauzet, F.: 2018, Magnetic cage and rope as the key for solar eruptions. *Nature* **554**(7691), 211. DOI. ADS.

Aulanier, G., Démoulin, P.: 1998, 3-D magnetic configurations supporting prominences. I. The natural presence of lateral feet. *Astron. Astrophys.* **329**, 1125. ADS.

Aulanier, G., Török, T., Démoulin, P., DeLuca, E.E.: 2010, Formation of torus-unstable flux ropes and electric currents in erupting sigmoids. *Astrophys. J.* **708**, 314. DOI. ADS.

Berger, T.E., Shine, R.A., Slater, G.L., Tarbell, T.D., Title, A.M., Okamoto, T.J., Ichimoto, K., Katsukawa, Y., Suematsu, Y., Tsuneta, S., Lites, B.W., Shimizu, T.: 2008, Hinode SOT observations of solar quiescent prominence dynamics. *Astrophys. J. Lett.* **676**(1), L89. DOI. ADS.

Bommier, V., Sahal-Brechot, S., Leroy, J.L.: 1986, The linear polarization of hydrogen H-beta radiation and the joint diagnostic of magnetic field vector and electron density in quiescent prominences. I - the magnetic field. II - the electron density. *Astron. Astrophys.* **156**(1–2), 79. ADS.

Chae, J., Ahn, K., Lim, E.-K., Choe, G.S., Sakurai, T.: 2008, Persistent horizontal flows and magnetic support of vertical threads in a quiescent prominence. *Astrophys. J. Lett.* **689**(1), L73. DOI. ADS.

Chandra, R., Gupta, G.R., Mulay, S., Tripathi, D.: 2015, Sunspot waves and triggering of homologous active region jets. *Mon. Not. Roy. Astron. Soc.* **446**, 3741. DOI. ADS.

Chandra, R., Mandrini, C.H., Schmieder, B., Joshi, B., Cristiani, G.D., Cremades, H., Pariat, E., Nuevo, F.A., Srivastava, A.K., Uddin, W.: 2017a, Blowout jets and impulsive eruptive flares in a bald-patch topology. *Astron. Astrophys.* **598**, A41. DOI. ADS.

Chandra, R., Filippov, B., Joshi, R., Schmieder, B.: 2017b, Two-step filament eruption during 14 - 15 March 2015. *Solar Phys.* **292**(6), 81. DOI. ADS.

Chen, H., Ma, S., Zhang, J.: 2013, Overlying extreme-ultraviolet arcades preventing eruption of a filament observed by AIA/SDO. *Astrophys. J.* **778**(1), 70. DOI. ADS.

Chen, J., Su, J., Yin, Z., Priya, T.G., Zhang, H., Liu, J., Xu, H., Yu, S.: 2015, Recurrent solar jets induced by a satellite spot and moving magnetic features. *Astrophys. J.* **815**(1), 71. DOI. ADS.

Chen, H., Duan, Y., Yang, J., Yang, B., Dai, J.: 2018, Witnessing tether-cutting reconnection at the onset of a partial eruption. *Astrophys. J.* **869**(1), 78. DOI. ADS.

Cheng, X., Hao, Q., Ding, M.D., Liu, K., Chen, P.F., Fang, C., Liu, Y.D.: 2015, A two-ribbon white-light flare associated with a failed solar eruption observed by ONSET, SDO, and IRIS. *Astrophys. J.* **809**(1), 46. DOI. ADS.

De Pontieu, B., Title, A.M., Lemen, J.R., Kushner, G.D., Akin, D.J., Allard, B., Berger, T., Boerner, P., Cheung, M., Chou, C., Drake, J.F., Duncan, D.W., Freeland, S., Heyman, G.F., Hoffman, C., Hurlburt, N.E., Lindgren, R.W., Mathur, D., Rehse, R., Sabolish, D., Seguin, R., Schrijver, C.J., Tarbell, T.D., Wülser, J.-P., Wolfson, C.J., Yanari, C., Mudge, J., Nguyen-Phuc, N., Timmons, R., van Bezooijen, R., Weingrod, I., Brookner, R., Butcher, G., Dougherty, B., Eder, J., Knagenhjelm, V., Larsen, S., Mansir, D., Phan, L., Boyle, P., Cheimets, P.N., DeLuca, E.E., Golub, L., Gates, R., Hertz, E., McKillop, S., Park, S., Perry, T., Podgorski, W.A., Reeves, K., Saar, S., Testa, P., Tian, H., Weber, M., Dunn, C., Eccles, S., Jaeggli, S.A., Kankelborg, C.C., Mashburn, K., Pust, N., Springer, L., Carvalho, R., Kleint, L., Marmie, J., Mazmanian, E., Pereira, T.M.D., Sawyer, S., Strong, J., Worden, S.P., Carlsson, M., Hansteen, V.H., Leenaarts, J., Wiesmann, M., Aloise, J., Chu, K.-C., Bush, R.I., Scherrer, P.H., Brekke, P., Martinez-Sykora, J., Lites, B.W., McIntosh, S.W., Uitenbroek, H., Okamoto, T.J., Gummin, M.A., Auker, G., Jerram, P., Pool, P., Waltham, N.: 2014, The Interface Region Imaging Spectrograph (IRIS). *Solar Phys.* **289**(7), 2733. DOI. ADS.

Démoulin, P., Bagala, L.G., Mandrini, C.H., Henoux, J.C., Rovira, M.G.: 1997, *Astron. Astrophys.* **325**, 305.

Deng, M., Welsch, B.T.: 2017, The roles of reconnected flux and overlying fields in CME speeds. *Solar Phys.* **292**(1), 17. DOI. ADS.

Devi, P., Démoulin, P., Chandra, R., Joshi, R., Schmieder, B., Joshi, B.: 2021, Observations of a prominence eruption and loop contraction. *Astron. Astrophys.* **647**, A85. DOI. ADS.

Fan, Y.: 2015, In: Vial, J.-C., Engvold, O. (eds.) *MHD Equilibria and Triggers for Prominence Eruption* **415**, 297. DOI. ADS.

Fan, Y., Gibson, S.E.: 2003, The emergence of a twisted magnetic flux tube into a preexisting coronal arcade. *Astrophys. J. Lett.* **589**(2), L105. DOI. ADS.

Filippov, B.P.: 2020, Failed eruptions of solar filaments. *Astron. Rep.* **64**(3), 272. DOI. ADS.

Filippov, B.: 2021, Mass of prominences experiencing failed eruptions. *Publ. Astron. Soc. Aust.* **38**, e018. DOI. ADS.

Gibson, S.E.: 2018, Solar prominences: theory and models. Fleshing out the magnetic skeleton. *Living Rev. Solar Phys.* **15**(1), 7. DOI. ADS.

Green, L.M., López fuentes, M.C., Mandrini, C.H., Démoulin, P., Van Driel-Gesztelyi, L., Culhane, J.L.: 2002, The magnetic helicity budget of a cme-prolific active region. *Solar Phys.* **208**, 43. DOI. ADS.

Guo, J., Liu, Y., Zhang, H., Deng, Y., Lin, J., Su, J.: 2010, A flux rope eruption triggered by jets. *Astrophys. J.* **711**, 1057. DOI. ADS.

Harvey, K., Harvey, J.: 1973, Observations of moving magnetic features near sunspots. *Solar Phys.* **28**(1), 61. DOI. ADS.

Hong, J., Jiang, Y., Zheng, R., Yang, J., Bi, Y., Yang, B.: 2011, A micro coronal mass ejection associated blowout extreme-ultraviolet jet. *Astrophys. J. Lett.* **738**, L20. DOI. ADS.

Howard, R.A., Moses, J.D., Vourlidas, A., Newmark, J.S., Socker, D.G., Plunkett, S.P., et al.: 2008, Sun Earth connection coronal and heliospheric investigation (SECCHI). *Space Sci. Rev.* **136**, 67. DOI. ADS.

Joshi, N.C., Srivastava, A.K., Filippov, B., Uddin, W., Kayshap, P., Chandra, R.: 2013, A study of a failed coronal mass ejection core associated with an asymmetric filament eruption. *Astrophys. J.* **771**(1), 65. DOI. ADS.

Joshi, R., Schmieder, B., Tei, A., Aulanier, G., Lörinčík, J., Chandra, R., Heinzel, P.: 2021, Multi-thermal atmosphere of a mini-solar flare during magnetic reconnection observed with IRIS. *Astron. Astrophys.* **645**, A80. DOI. ADS.

Karpen, J.T., Antiochos, S.K., DeVore, C.R.: 2012, The mechanisms for the onset and explosive eruption of coronal mass ejections and eruptive flares. *Astrophys. J.* **760**, 81. DOI. ADS.

Labrosse, N., Heinzel, P., Vial, J.-C., Kucera, T., Parenti, S., Gunár, S., Schmieder, B., Kilper, G.: 2010, Physics of solar prominences: I—spectral diagnostics and non-LTE modelling. *Space Sci. Rev.* **151**(4), 243. DOI. ADS.

Lemen, J.R., Title, A.M., Akin, D.J., Boerner, P.F., Chou, C., Drake, J.F., Duncan, D.W., Edwards, C.G., Friedlaender, F.M., Heyman, G.F., Hurlburt, N.E., Katz, N.L., Kushner, G.D., Levay, M., Lindgren, R.W., Mathur, D.P., McFeaters, E.L., Mitchell, S., Rehse, R.A., Schrijver, C.J., Springer, L.A., Stern, R.A., Tarbell, T.D., Wuelser, J.-P., Wolfson, C.J., Yanari, C., Bookbinder, J.A., Cheimets, P.N., Caldwell, D., Deluca, E.E., Gates, R., Golub, L., Park, S., Podgorski, W.A., Bush, R.I., Scherrer, P.H., Gummin, M.A., Smith, P., Auker, G., Jerram, P., Pool, P., Soufli, R., Windt, D.L., Beardsley, S., Clapp, M., Lang, J., Waltham, N.: 2012, The Atmospheric Imaging Assembly (AIA) on the Solar Dynamics Observatory (SDO). *Solar Phys.* **275**, 17. DOI. ADS.

Leroy, J.L., Bommier, V., Sahal-Brechot, S.: 1983, The magnetic field in the prominences of the polar crown. *Solar Phys.* **83**(1), 135. DOI. ADS.

Levens, P.J., Schmieder, B., López Ariste, A., Labrosse, N., Dalmasse, K., Gelly, B.: 2016, Magnetic field in atypical prominence structures: bubble, tornado, and eruption. *Astrophys. J.* **826**(2), 164. DOI. ADS.

Liu, Y., Su, J., Xu, Z., Lin, H., Shibata, K., Kurokawa, H.: 2009, New observation of failed filament eruptions: the influence of asymmetric coronal background fields on solar eruptions. *Astrophys. J. Lett.* **696**(1), L70. DOI. ADS.

Liu, L., Wang, Y., Zhou, Z., Dissauer, K., Temmer, M., Cui, J.: 2018, A comparative study between a failed and a successful eruption initiated from the same polarity inversion line in AR 11387. *Astrophys. J.* **858**(2), 121. DOI. ADS.

López Ariste, A., Aulanier, G., Schmieder, B., Sainz Dalda, A.: 2006, First observation of bald patches in a filament channel and at a barb endpoint. *Astron. Astrophys.* **456**(2), 725. DOI. ADS.

López Fuentes, M., Mandrini, C.H., Poisson, M., Démoulin, P., Cristiani, G., López, F.M., Luoni, M.L.: 2018, Physical processes involved in the EUV "surge" event of 9 May 2012. *Solar Phys.* **293**(12), 166. DOI. ADS.

Mackay, D.H., Karpen, J.T., Ballester, J.L., Schmieder, B., Aulanier, G.: 2010, Physics of solar prominences: II–magnetic structure and dynamics. *Space Sci. Rev.* **151**, 333. DOI. ADS.

Mandrini, C.H., Démoulin, P., Schmieder, B., Deluca, E.E., Pariat, E., Uddin, W.: 2006, Companion event and precursor of the X17 flare on 28 October 2003. *Solar Phys.* **238**, 293. DOI. ADS.

Mandrini, C.H., Schmieder, B., Démoulin, P., Guo, Y., Cristiani, G.D.: 2014, Topological analysis of emerging bipole clusters producing violent solar events. *Solar Phys.* **289**(6), 2041. DOI. ADS.

Martin, S.F.: 1998, Conditions for the formation and maintenance of filaments (invited review). *Solar Phys.* **182**(1), 107. DOI. ADS.

Moore, R.L., Sterling, A.C., Panesar, N.K.: 2018, Onset of the magnetic explosion in solar polar coronal X-ray jets. *Astrophys. J.* **859**, 3. DOI. ADS.

Morgan, H., Druckmüller, M.: 2014, Multi-scale Gaussian normalization for solar image processing. *Solar Phys.* **289**(8), 2945. DOI. ADS.

Nisticò, G., Polito, V., Nakariakov, V.M., Del Zanna, G.: 2017, Multi-instrument observations of a failed flare eruption associated with MHD waves in a loop bundle. *Astron. Astrophys.* **600**, A37. DOI. ADS.

Panesar, N.K., Sterling, A.C., Moore, R.L.: 2017, Magnetic flux cancellation as the origin of solar quiet-region pre-jet minifilaments. *Astrophys. J.* **844**, 131. DOI. ADS.

Poisson, M., Bustos, C., López Fuentes, M., Mandrini, C.H., Cristiani, G.D.: 2020, Two successive partial mini-filament confined ejections. *Adv. Space Res.* **65**(6), 1629. DOI. ADS.

Ruan, G., Schmieder, B., Masson, S., Mein, P., Mein, N., Aulanier, G., Chen, Y.: 2019, Bi-directional reconnection outflows in an active region. *Astrophys. J.* **883**(1), 52. ADS.

Scherrer, P.H., Schou, J., Bush, R.I., Kosovichev, A.G., Bogart, R.S., Hoeksema, J.T., Liu, Y., Duvall, T.L., Zhao, J., Title, A.M., Schrijver, C.J., Tarbell, T.D., Tomczyk, S.: 2012, The Helioseismic and Magnetic Imager (HMI) investigation for the Solar Dynamics Observatory (SDO). *Solar Phys.* **275**, 207. DOI. ADS.

Schmieder, B.: 2022, Solar jets: SDO and IRIS observations in the perspective of new MHD simulations. *Front. Astron. Space Sci.* **9**, 820183. DOI. arXiv. ADS.

Schmieder, B., Démoulin, P., Aulanier, G.: 2013, Solar filament eruptions and their physical role in triggering coronal mass ejections. *Adv. Space Res.* **51**(11), 1967. DOI. ADS.

Schmieder, B., Mein, N., Deng, Y., Dumitrache, C., Malherbe, J.-M., Staiger, J., Deluca, E.E.: 2004, Magnetic changes observed in the formation of two filaments in a complex active region: TRACE and MSDP observations. *Solar Phys.* **223**(1–2), 119. DOI. ADS.

Schmieder, B., Aulanier, G., Mein, P., López Ariste, A.: 2006, Evolving photospheric flux concentrations and filament dynamic changes. *Solar Phys.* **238**(2), 245. DOI. ADS.

Schmieder, B., Tian, H., Kucera, T., López Ariste, A., Mein, N., Mein, P., Dalmasse, K., Golub, L.: 2014, Open questions on prominences from coordinated observations by IRIS, Hinode, SDO/AIA, THEMIS, and the Meudon/MSDP. *Astron. Astrophys.* **569**, A85. DOI. ADS.

Schmieder, B., Zapiór, M., López Ariste, A., Levens, P., Labrosse, N., Gravet, R.: 2017, Reconstruction of a helical prominence in 3D from IRIS spectra and images. *Astron. Astrophys.* **606**, A30. DOI. ADS.

Shen, Y.: 2021, Observation and modelling of solar jets. *Proc. Roy. Soc. London Ser. A* **477**(2246), 217. DOI. ADS.

Shen, Y.-D., Liu, Y., Liu, R.: 2011, A time series of filament eruptions observed by three eyes from space: from failed to successful eruptions. *Res. Astron. Astrophys.* **11**(5), 594. DOI. ADS.

Shen, Y., Liu, Y., Su, J.: 2012, Sympathetic partial and full filament eruptions observed in one solar breakout event. *Astrophys. J.* **750**(1), 12. DOI. ADS.

Shen, Y., Liu, Y., Liu, Y.D., Chen, P.F., Su, J., Xu, Z., Liu, Z.: 2015, Fine magnetic structure and origin of counter-streaming mass flows in a quiescent solar prominence. *Astrophys. J. Lett.* **814**(1), L17. DOI. ADS.

Shen, Y., Liu, Y.D., Su, J., Qu, Z., Tian, Z.: 2017, On a solar blowout jet: driving mechanism and the formation of cool and hot components. *Astrophys. J.* **851**, 67. DOI. ADS.

Shen, Y., Liu, Y., Liu, Y.D., Su, J., Tang, Z., Miao, Y.: 2018, Homologous large-amplitude nonlinear fast-mode magnetosonic waves driven by recurrent coronal jets. *Astrophys. J.* **861**(2), 105. DOI. ADS.

Shen, Y., Qu, Z., Yuan, D., Chen, H., Duan, Y., Zhou, C., Tang, Z., Huang, J., Liu, Y.: 2019, Stereoscopic observations of an erupting mini-filament-driven two-sided-loop jet and the applications for diagnosing a filament magnetic field. *Astrophys. J.* **883**(1), 104. DOI. ADS.

Stenborg, G., Vourlidas, A., Howard, R.A.: 2008, A fresh view of the extreme-ultraviolet corona from the application of a new image-processing technique. *Astrophys. J.* **674**(2), 1201. DOI. ADS.

Sterling, A.C., Moore, R.L., Falconer, D.A., Adams, M.: 2015, Small-scale filament eruptions as the driver of X-ray jets in solar coronal holes. *Nature* **523**, 437. DOI. ADS.

Sterling, A.C., Moore, R.L., Falconer, D.A., Panesar, N.K., Akiyama, S., Yashiro, S., Gopalswamy, N.: 2016, Minifilament eruptions that drive coronal jets in a solar active region. *Astrophys. J.* **821**, 100. DOI. ADS.

Tandberg-Hanssen, E.: 1995, *The Nature of Solar Prominences* **199**. DOI. ADS.

Thalmann, J.K., Su, Y., Temmer, M., Veronig, A.M.: 2015, The confined X-class flares of solar active region 2192. *Astrophys. J. Lett.* **801**(2), L23. DOI. ADS.

Tian, Z., Liu, Y., Shen, Y., Elmhamdi, A., Su, J., Liu, Y.D., Kordi, A.S.: 2017, Successive two-sided loop jets caused by magnetic reconnection between two adjacent filamentary threads. *Astrophys. J.* **845**(2), 94. DOI. ADS.

Török, T., Kliem, B.: 2005, *Astrophys. J. Lett.* **630**, L97.

Tóth, G., van der Holst, B., Huang, Z.: 2011, Obtaining potential field solutions with spherical harmonics and finite differences. *Astrophys. J.* **732**, 102. DOI. ADS.

van Ballegooijen, A.A.: 2004, Observations and modeling of a filament on the sun. *Astrophys. J.* **612**(1), 519. DOI. ADS.

van Ballegooijen, A.A., Martens, P.C.H.: 1989, Formation and eruption of solar prominences. *Astrophys. J.* **343**, 971. DOI. ADS.

van Driel-Gesztelyi, L., Green, L.M.: 2015, Evolution of active regions. *Living Rev. Solar Phys.* **12**(1), 1. DOI. ADS.

Wang, Y.-M., Muglach, K.: 2007, On the formation of filament channels. *Astrophys. J.* **666**(2), 1284. DOI. ADS.

Webb, D.F., Howard, T.A.: 2012, Coronal mass ejections: observations. *Living Rev. Solar Phys.* **9**, 3. DOI. ADS.

Wuelser, J.-P., Lemen, J.R., Tarbell, T.D., Wolfson, C.J., Cannon, J.C., Carpenter, B.A., Duncan, D.W., Gradwohl, G.S., Meyer, S.B., Moore, A.S., Navarro, R.L., Pearson, J.D., Rossi, G.R., Springer, L.A., Howard, R.A., Moses, J.D., Newmark, J.S., Delaboudiniere, J.-P., Artzner, G.E., Auchere, F., Bougnet, M., Bouyries, P., Bridou, F., Clotaire, J.-Y., Colas, G., Delmotte, F., Jerome, A., Lamare, M., Mercier, R., Mullot, M., Ravet, M.-F., Song, X., Bothmer, V., Deutsch, W.: 2004, EUVI: the STEREO-SECCHI extreme ultraviolet imager. In: Fineschi, S., Gummin, M.A. (eds.) *Telescopes and Instrumentation for Solar Astrophysics*, *Society of Photo-Optical Instrumentation Engineers (SPIE) Conference Series* **5171**, 111. DOI. ADS.

Wyper, P.F., Antiochos, S.K., DeVore, C.R.: 2017, A universal model for solar eruptions. *Nature* **544**(7651), 452. DOI. ADS.

Wyper, P.F., DeVore, C.R., Antiochos, S.K.: 2018, A breakout model for solar coronal jets with filaments. *Astrophys. J.* **852**, 98. DOI. ADS.

Xue, Z., Yan, X., Zhao, L., Xiang, Y., Yang, L., Guo, Y.: 2016, Failed eruptions of two intertwining small-scale filaments. *Publ. Astron. Soc. Japan* **68**(1), 7. DOI. ADS.

Xue, Z., Yan, X., Yang, L., Wang, J., Zhao, L.: 2017, Observing formation of flux rope by tether-cutting reconnection in the sun. *Astrophys. J. Lett.* **840**(2), L23. DOI. ADS.

Yang, S., Zhang, J.: 2018, Mini-filament eruptions triggering confined solar flares observed by ONSET and SDO. *Astrophys. J. Lett.* **860**, L25. DOI. ADS.

Yang, B., Jiang, Y., Yang, J., Yu, S., Xu, Z.: 2016, The rapid formation of a filament caused by magnetic reconnection between two sets of dark threadlike structures. *Astrophys. J.* **816**(1), 41. DOI. ADS.

Zuccarello, F.P., Aulanier, G., Gilchrist, S.A.: 2016, The apparent critical decay index at the onset of solar prominence eruptions. *Astrophys. J. Lett.* **821**(2), L23. DOI. ADS.

Authors and Affiliations

Reetika Joshi[1,2,3] [iD] · **Cristina H. Mandrini[4]** [iD] · **Ramesh Chandra[3]** [iD] ·
Brigitte Schmieder[5,6,7] [iD] · **Germán D. Cristiani[4]** [iD] · **Cecilia Mac Cormack[4]** [iD] ·
Pascal Démoulin[5,8] [iD] · **Hebe Cremades[9,10]** [iD]

✉ R. Joshi
reetika.joshi@astro.uio.no

C.H. Mandrini
mandrini@iafe.uba.ar

R. Chandra
rchandra.ntl@gmail.com

B. Schmieder
Brigitte.Schmieder@obspm.fr

G.D. Cristiani
gcristiani@gmail.com

C. Mac Cormack
ceciliamaccormack@gmail.com

P. Démoulin
Pascal.Demoulin@obspm.fr

H. Cremades
hebe.cremades@gmail.com

1   Institute of Theoretical Astrophysics, University of Oslo, P.O. Box 1029 Blindern, N-0315 Oslo, Norway

2   Rosseland Centre for Solar Physics, University of Oslo, P.O. Box 1029 Blindern, N-0315 Oslo, Norway

3   Department of Physics, DSB Campus, Kumaun University, Nainital 263-001, India

4   Instituto de Astronomía y Física del Espacio, IAFE, UBA-CONICET, CC.67, Suc.28,1428 Buenos Aires, Argentina

5   LESIA, Observatoire de Paris, Université PSL, CNRS, Sorbonne Université, Université de Paris, 5 place Jules Janssen, 92190 Meudon, France

6   Centre for Mathematical Plasma Astrophysics, Dept. of Mathematics, KU Leuven, 3001 Leuven, Belgium

7   SUPA, School of Physics & Astronomy, University of Glasgow, G12 8QQ Glasgow, UK

8   Laboratoire Cogitamus, rue Descartes, 75005 Paris, France

9   Grupo de Estudios en Heliofísica de Mendoza, Facultad de Ingeniería, Universidad de Mendoza, 5500 Mendoza, Argentina

10   Consejo Nacional de Investigaciones Científicas y Técnicas, C1425FQB Ciudad Autónoma de Buenos Aires, Argentina